IOWA STATE UNIVERSITY
Digital Repository

Graduate Theses and Dissertations

Iowa State University Capstones, Theses and Dissertations

2015

Computational design of new scintillator chemistries and defect structures

Hyung jin Kim
Iowa State University

Follow this and additional works at: https://lib.dr.iastate.edu/etd

 Part of the Materials Science and Engineering Commons, and the Mechanics of Materials Commons

Recommended Citation
Kim, Hyung jin, "Computational design of new scintillator chemistries and defect structures" (2015). *Graduate Theses and Dissertations*. 14395.
https://lib.dr.iastate.edu/etd/14395

This Thesis is brought to you for free and open access by the Iowa State University Capstones, Theses and Dissertations at Iowa State University Digital Repository. It has been accepted for inclusion in Graduate Theses and Dissertations by an authorized administrator of Iowa State University Digital Repository. For more information, please contact digirep@iastate.edu.

Computational design of new scintillator chemistries and defect structures

by

Hyung jin Kim

A thesis submitted to the graduate faculty

in partial fulfillment of the requirements for the degree of

MASTER OF SCIENCE

Major: Materials Science and Engineering

Program of Study Committee:
Krishna Rajan, Major Professor
Kristen Constant
Ganesh Balasubramanian

Iowa State University

Ames, Iowa

2015

Copyright © Hyung jin Kim, 2015. All rights reserved.

DEDICATION

To my parents, my sister and uncle Uk-keun.

TABLE OF CONTENTS

LIST OF FIGURES

Page

LIST OF TABLES

ACKNOWLEDGEMENTS

I would like to acknowledge my advisor professor Rajan for making this research possible and supporting me in every way. Also I would like to thank professor Constant and professor Balasubramanian for agreeing to serve as my committee members and for being patient and supportive of me.

Special thanks to Dr. Scott Broderick for all the helps and answering questions for me every day. Thanks to Dr. Rupa Dumpala for her caring advices and my fellow MS lab mates Sri and Pallavi for their company.

I am also grateful to Hyun yong Lee as this thesis document work would not have been without her help.

ABSTRACT

The focus of this thesis is computationally designing inorganic scintillators previously predicted by informatics, which have not been validated computationally. Density Functional Theory (DFT) calculations were performed to (1) select garnet host lattices that are good scintillators, thereby down selecting from compounds previously identified via informatics, and (2) identify co-dopant chemistries in perovskites which enhance scintillator property. In this thesis, the property of focus is bandgap, which in general has an inverse correlation to light yield. The total energy code Cambridge Sequential Total Energy Package (CASTEP) was used for performing DFT calculations, taking advantage of its speed in modeling the electronic structure of the complex inorganic scintillators. From our calculations, $Tb_3Al_2Ga_3O_{12}$ was identified as forming a stable garnet structure and having a modeled direct bandgap corresponding with light yield better than other similar garnet host lattices. Further, from our calculations, we find four co-dopant chemistries which improve the bandgap from singly doped perovskites.

CHAPTER 1

INTRODUCTION

1.1 Objective

The focus of this thesis is computationally designing inorganic scintillators previously predicted by informatics, which have not been validated computationally. Density Functional Theory (DFT) calculations were performed to select garnet host lattices that are good scintillators, thereby down selecting from compounds previously identified via informatics. Another set of DFT calculations were also performed on co-dopant chemistries to identify the best co-dopant combinations for scintillator compound. DFT calculations were performed to calculate the band gap which is the primary parameter for defining the quality of the scintillator as band gap has well-known inverse correlation with light yield.

1.2. Background of Scintillator

1.2.1. What is a Scintillator?

A scintillator is a material that emits light during the de-excitation process that was caused by ionization produced by charged particles. Scintillation is a kind of luminescence caused by ionizing radiation. Luminescence is classified as a cold body radiation because the emission of light is caused by a source without involving heat such as chemical or electrical energy, stress on a crystal or subatomic motions within the crystal. When luminescent materials

are struck by an incoming particle they absorb the energy of the particle and scintillate, in other words, re-emit the absorbed energy as light. For some cases the excited state is metastable where the relaxation of the excited state coming back down to the lower state is delayed ranging from few nanoseconds to hours for different materials.

1.2.2. History of Scintillator

Scintillation is a phenomenon where light of a characteristic wavelength of a material is emitted after absorbing radiation. Scintillation phenomenon has been used to detect radiation for over a hundred years and they have major contribution to the development of modern physics. In early 1900s, E. Rutherford observed alpha particles and many consider this event as the beginning of modern nuclear physics. This observation was made possible by visual observation of zinc sulfide scintillator. In the early stage of scintillator use, ZnS and $CaWO_4$ were the most popular scintillator materials for nuclear physics experiments. After the Second World War, intensive research on atomic projects led to the advance in ionizing radiation detection technique as well as scintillation counters. Guided by the advance in experimental physics, and especially with appearance of the photoelectric multipliers, researchers quickly learnt that scintillating materials were ideal for detecting elementary particles and study them [1.1].

In a short period of time from 1947 to 1951 scintillation phenomenon was reported in various kinds of materials including organic and inorganic crystalline media [1.2-1.5], polymeric compounds [1.6], fluids [1.7-1.10] and even with gases [1.11-1.12].

In this thesis, the focus is on the inorganic scintillator materials and Figure 1.1 shows the series of discoveries of important inorganic scintillator materials in the past century [1.13]. These are listed as important because they were commercialized and became popular or they sparked further developments or hinted new directions for research.

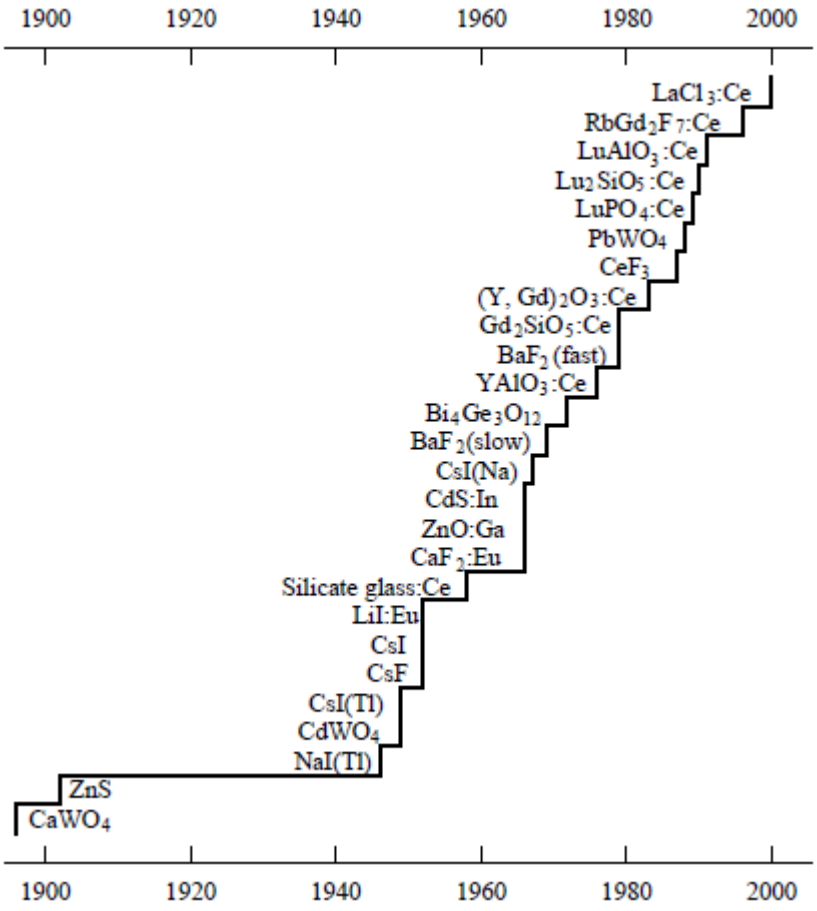

Figure 1.1. History of discovery of inorganic scintillator materials. [1.13]

The different periods exist in the scintillator discovery history. The discoveries of the earliest scintillators (i.e. $CaWO_4$ and ZnS) are in included the first period. Calcium Tungstate was first used as a scintillator only a year after Rontgen's X-rays discovery. Becquerel used uranyl salts to discover radioactivity. Crookes used ZnS scintillators to count radioactivity and

Rutherford also used ZnS to study alpha particles. The introduction of naphthalene scintillators and the advance of photomultiplier tubes happened just before the second period.

The second period started with the thallium-activated NaI developed by Hofstadter. During the rush of scintillator exploration most of the pure scintillator properties and activated akali halide scintillator properties were studied.In 1950s, neutron detection technique using compounds containing Li was developed and the first Ce activated glass scintillators were also developed. In the following decades new scintillator materials appeared at a steady rate including BaF_2 with fast core-valence luminescence.

In the past two decades, large demands of scintillators for precision calorimetry in high energy physics and for high light output scintillators for medical imaging, geophysical exploration, and numerous other scientific and industrial applications [1.1] led to rapid growth in the scintillator materials research.

Figure 1.2 is a scatter plot of decay time versus light yield data for many different inorganic scintillator materials including garnets and perovskite classes of materials taken from the scintillation data base [1.14-1.15]. Figure 1.2 shows the current status of the scintillator performance along with the target design direction of this work which is to have high light yield and fast decay time and these two are the most important properties of scintillators.

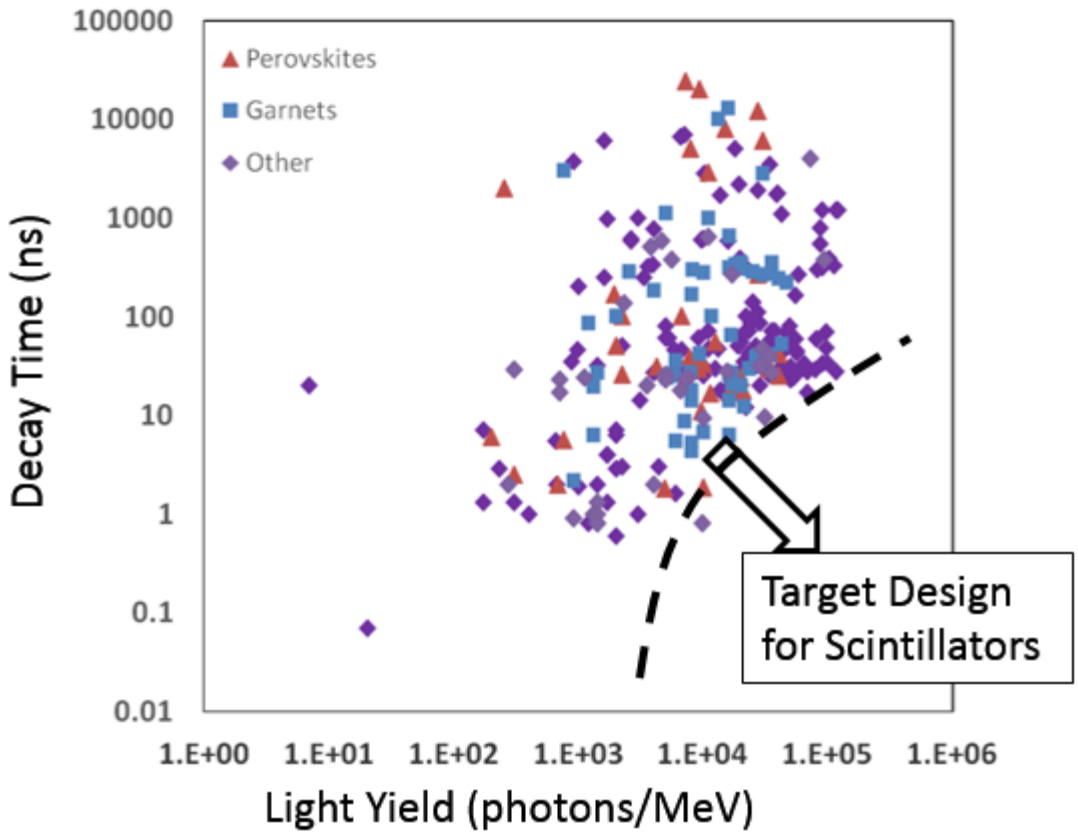

Figure 1.2. A scatter plot of decay time versus light yield of contemporary inorganic scintillators. Decay time is in nanoseconds and light yield is photons per MeV. The target design direction of this work is towards high light yield and fast decay time.

1.2.3. Mechanism of Inorganic Scintillator

In simple words, the scintillation process can be considered as the process where the energy of incident gamma ray converting to many number of photons with low energy. After the scintillator has been hit by a radiation it tries to relax to a new equilibrium state from a non-equilibrium state. The relaxation occurs with number of elementary processes including the

primary electronic excitation which produces many more secondary excitation such as electrons, holes, plasmons and photons. These secondary excitations in turn produces a number of thermalized electron-hole (e-h) pairs along with low energy excitons which eventually turns into light photons. [1.16]

Typically, the scintillation mechanism can be broken down into four steps [1.17]:

1. The absorption of a γ-rays which creates a primary electron-hole pair
2. The production of multiple secondary electrons and holes and their thermalization process
3. Energy transport from the electrons and holes to luminescence centers
4. Emission of radiation from the luminescence center.

1.2.3.1. Absorption of γ-rays

When electromagnetic radiation interacts with matter, the radiation is completely or absorbed or partially absorbed. The three fundamental electromagnetic interaction mechanisms in the rage of few keV to few MeV are the photoelectric effect, Compton scattering and electron-positron pair formation. The interaction cross section for each mechanism is energy dependent, photoelectric effect and Compton scattering are dominant at low and medium range of energy and pair formation being dominant at high energy above 1.02 MeV which is the rest mass energy of electron and positron. In photoelectric absorption process, γ-ray is absorbed by a bound electron and usually a K-shell or L-shell electron is ejected from the atom. For electrons with energy above the K-absorption edge, the scattering cross section of an atom is proportional to Z^n/E^k. The scattering cross section of an atom is a mathematical area that

determines the probability of radiation being scattered by the atom or the scattering center. Here *Z* is the atomic number, *E* is the energy of the radiation and with constant n varying from 4 to 5 and another constant k varying from 2 to 4. In the case of Compton scattering the cross section is proportional to Z/E. For radiation energy above 1.02MeV pair production dominates and the cross section per atom is proportional to ~$Z^2 ln(2E/m_0c^2)$ with m_0c^2 of 0.511MeV for the rest mass energy of an electron.

For a compound that consists of different kinds of atoms the absorption coefficient is determined by the cross section description from the above paragraph and the number of atoms per unit volume.

1.2.3.2. Electron-hole Pair Multiplication

When the ionizing radiation is absorbed by the material primary electron and hole pair with high energy is generated. These primary e-h pair generates secondary e-h pairs and the number of e-h pairs grows quickly. This multiplication continues until there is no energy left to ionize more electrons. The excess energy possessed by this e-h pair is dissipated through thermalization. In general, electron-hole pair creation energy required after the high energy radiation absorption is about two to three times that of a bandgap energy depending on the valence bandwidth. The amount of time that this process takes is believe to be in the order of picoseconds.

1.2.3.3. Energy Transportation

The transfer of energy of e-h pair to the luminescence centers is followed by thermalization process. This stage also called the energy transport stage. The e-h pair can form excitons and they might get self-trapped in materials that are bonded ionically. These self-trapped charge or energy carriers can undergo different processes. Their energy can be transferred to the luminescence centers, losing the energy in a non-radiative way or they become lost by getting trapped near an undesired impurity or a defect. The chances for these difference processes depend on several factors. These factors include how far the interacting carriers are, how large the cross-section of the interaction is and how high temperature is. As a result of these factors, the scintillation properties change depending on the temperature and the luminescence center concentrations. On top of this, the transport efficiency can also be varied as the e-h pair density varies.

The sophistication involved with these transfer processes makes it hard to tell what the efficiency of the transport stage would be and it is probably why these processes are not yet well understood. The time scale of the transport can vary widely from picoseconds to milliseconds. Scintillators with prolonged transport stage exhibit scintillator afterglow phenomenon.

1.2.3.4. Luminescence

Luminescence is the final stage of the scintillation process. The energy within the crystal lattice that is initially given by the ionization radiation is given off in form of light in the luminescence center. The properties of luminescence center can be studied using optical characterization.

1.2.3.5. Efficiency

The efficiency of a scintillator is determined by the efficiency of three following stages. The electron-hole pair multiplication stage (which depends on the energy of the bandgap, E_g,), the energy transportation stage and the luminescence stage. The quantitative efficiencies for transportation stage and luminescence stage are denoted by S and Q respectively. Then the light yield of a scintillator, denoted by Y (in photons/MeV), can be expressed as:

$$\mathrm{Y} = \frac{10^6 SQ}{\beta E_g} \qquad (1.1)$$

The bandgap E_g is expressed in the units of eV and βE_g represents the energy required for the creation of one electron-hole pair.

Figure 1.3 is a re-plot of Figure 1.2 in terms of bandgap using the inverse correlation between the light yield and the band gap. The primary parameter considered in this thesis is the bandgap which can be calculated for potential new scintillators. The target design region is now colored in blue in Figure 1.3.

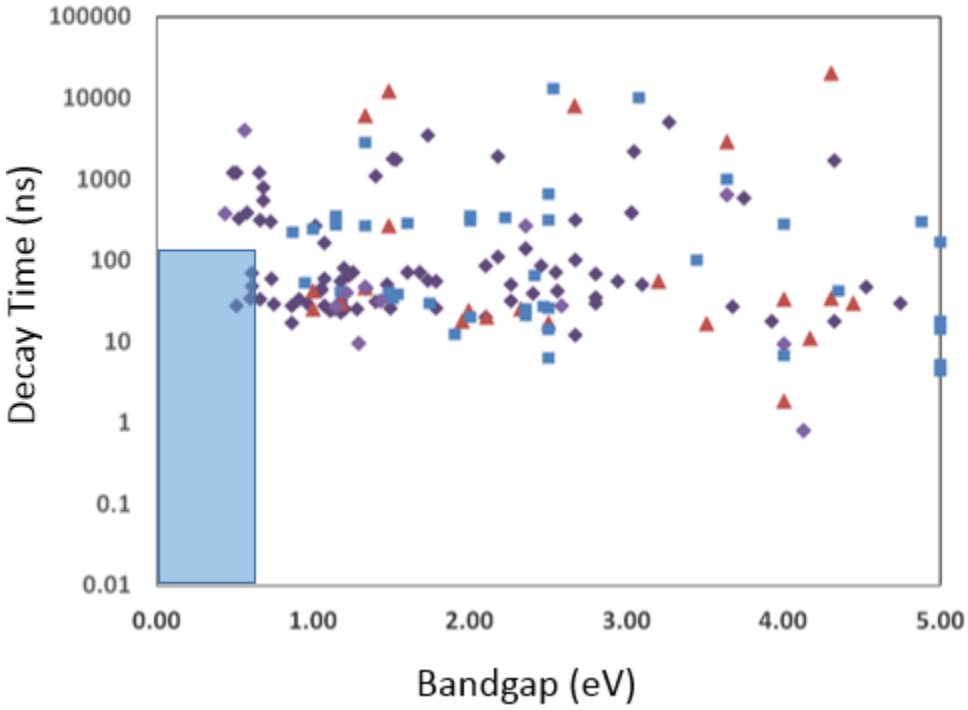

Figure 1.3. A scatter plot of decay time versus bangap of contemporary inorganic scintillators. Decay time is in nanoseconds and bandgap is in eV. The target design direction is now the blue region with fast decay time and low bandgap.

1.2.3.6. Decay Time

Decay time of a scintillator material is defined as the time between the introduction of radiation and the release of light, in other words how long an each cycle of scintillation process takes. Among the four stages of scintillation process, the energy transport stage and the luminescence center decay time takes much longer than the radiation absorption stage and the multiplication and thermalization stage of e-h pairs, Therefore, the energy transport stage and the luminescence stage are the rate determining stages of the time response. Moreover, the slowest one of those two slower stages will decide the decay time of the scintillator.

1.2.4. Considerations for the Search for New Scintillators

There are three main practical scintillation parameters that are relevant for choice of a known or the development of a new scintillator. The parameters are the light yield, decay time and γ-ray absorption power but the light yield and bandgap will be the parameters of focus in this thesis. From equation 1.1, it is suggested that materials with a small E_g has a potential of being a high light yield scintillator material. For materials being built of ions having a noble gas configuration, E_g decreases roughly along the series fluorides (9-12eV), oxides (5-9eV), chlorides (6-8eV), bromides (5-7eV), iodides (4-6eV), sulphides (2-5eV) and selenides (2-4eV) [1.17]. In the search for new scintillator materials, mainly oxides and fluorides gained attention. In this work, inorganic oxides classes of material systems were chosen to be studied.

1.3. Material Systems

The two material systems of focus are the garnets and the perovskites. Both of the systems are inorganic materials and they are commonly used scintillator host materials. In this thesis, two different design objectives are set for two material systems.

Garnets are a complex oxide with the general formula $X_3Y_2(ZO_3)_4$. Divalent cations usually occupy X the site, Trivalent cations occupy the Y site and silicon or Aluminum usually occupies the Z site. Garnets crystallize in cubic system

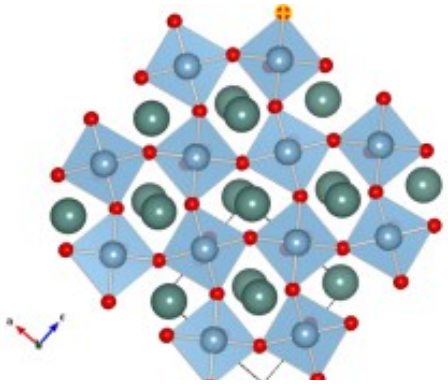

Figure 1.4 An example of garnet structure

with space group Ia3d and garnets are historically known to be good host lattices with significant interest in the literature [1.18-1.50]. For garnets, the objective is to design a host lattice with small bandgap and stability. Theoretical calculations were performed on 12 garnet chemistries which have never been explored previously.

Perovskites also have cubic structure with general formula of ABO_3. The A site, located at the corner of the lattice, is usually occupied with rare earth or alkaline metal. The B site, located at the center of the lattice, are occupied by metal elements or transitional metal elements. Perovskites crystallize in cubic system with space group Pbnm and perovskites also received gained significant attention in the literature [1.51-1.76]. For perovskites, the objective is to try different co-dopant combinations for small bandgap on $YAlO_3$ host lattice. Theoretical calculations were performed on 26 co-dopant chemistries with only 2 that have been previously explored.

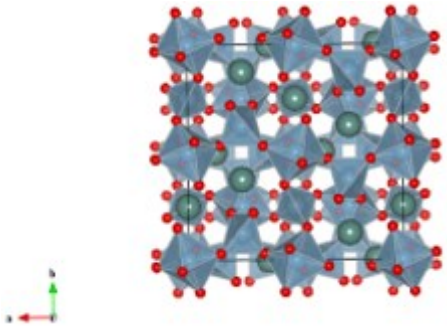

Figure 1.5. An example of perovskite structure.

1.4. Material Screening Logic

Figure 1.6 describes the material search logic of the project that this thesis work is a part of. Each sphere represents a possible garnet host lattice or a possible co-dopant combination pair for a perovskite host lattice. The search for ideal scintillator materials starts with all possible garnet and perovskite materials and chemistries. Then material screening steps

are applied for faster search of promising new materials. The first screening step was done earlier by our research group which was to do informatics analysis by data mining modeling to rapidly screen the material search space to identify a reduced number of potential new materials. Density functional theory calculations were performed to identify the best new scintillator materials after the number of candidates have been reduced. This second screening step is the focus of this thesis.

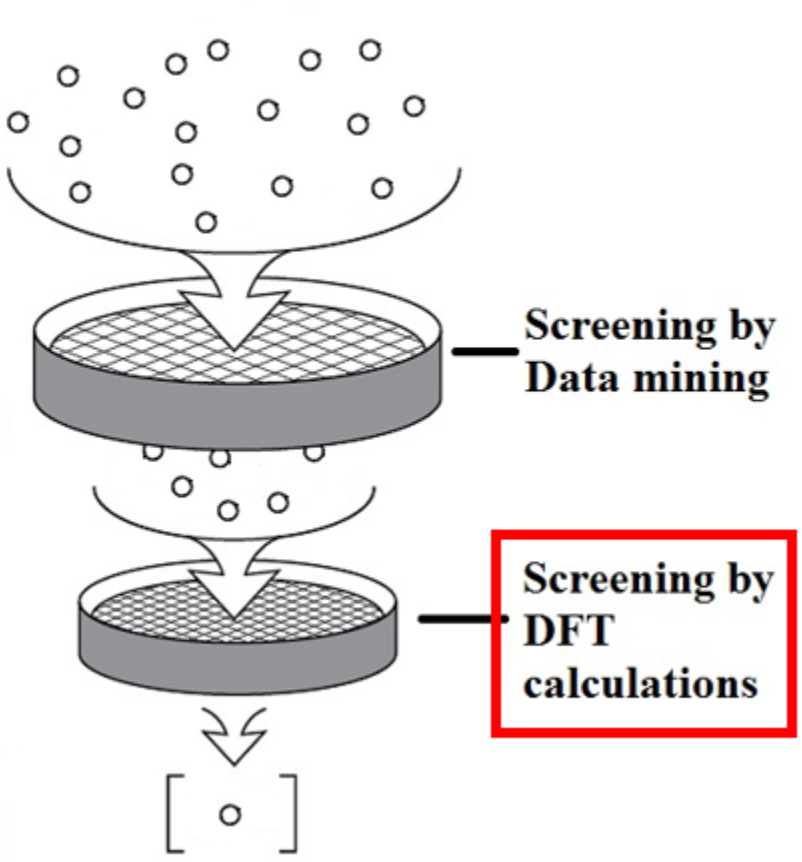

Figure 1.6. A schematic illustration of material search logic showing two screening steps. Each sphere represents a possible garnet host lattice or a possible co-dopant chemistry for $YAlO_3$ perovskite. Red square indicates the work of this thesis.

1.5. Outline of the Thesis

This thesis is organized in the following structure. Chapter 2 explains the necessary mathematical background knowledge on the density functional theory to run the DFT calculations. The background of the software called CASTEP (Cambridge Sequential Total Energy Package) and the methods that were used to run these calculations including the input parameters were explained in chapter 3 along with an example calculation. In chapter 4, the DFT calculation results for garnet host lattices are presented with band structure figures. In chapter 5, the DFT calculation results for co-doped perovskites are presented also with band structure figures. In the final chapter, the results were summarized with the conclusion of the thesis.

References

[1.1] P. Lecoq et al.: *Inorganic Scintillators for Detector Systems*: Netherlands (Springer, 2005)

[1.2] R. J. Moon: *Inorganic crystals for the detection of high energy particles and quanta*: Physical Review **73** 1210 (1948)

[1.3] H. Kallmann: *Quantitative measurements with scintillation counters*: Physiscal Review **75** 623–626 (1949)

[1.4] G. B. Collins , R.C. Hoyt: *Detection of beta-rays by scintillations*: Physical Review **73** 1259–1260 (1948)

[1.5] P. R. Bell: The use of anthrance as a scintillation counter. Physical Review **73** 1405–1406 (1948)

[1.6] M. G. Schorr, F. L. Torney: *Solid non-crystalline scintillation phosphors*: Proceedings of the Physical Society (London) Letters to the Editor. 474–475 (1950)

[1.7] H. Kallmann: *Scintillation counting with solutions*: Proceedings of the Physical Society (London) Letters to the Editor. 621–622 (1950)

[1.8] H. Kallmann, M. Furst: *Fluorescence of solutions bombarded with high energy radiation (energy transport in liquids*: Physical Review **79** 857–870 (1950)

[1.9] H. Kallmann, M. Furst: *Fluorescence of solutions bombarded with high energy radiation (energy transport in liquids)*: Part II. Physical Review **81** 853–864 (1951)

[1.10] H. Kallmann, M. Furst: *High energy induced fluorescence in organic liquid solutions (energy transport in liquids)*: Part III. Physical Review **85** 816–825 (1951)

[1.11] G. T. Reynolds: *Noble gas scintillation under electron excitation*: Nucleonics **6** 488–489 (1950)

[1.12] R. K. Swank: *Recent advances in theory of scintillation phosphors*: Nucleonics **12** 14–22 (1954)

[1.13] S. Derenzo et al.: *The quest for the ideal inorganic scintillator*: Nuclear Instruments and Methods in Physics Research A **505** 111-117 (2003)

[1.14] S. Derenzo et al.: *Scintillator database*: Lawrence Berkeley National Lab (http://scintillator.lbl.gov/) (Updated: Feb 2015) (Accessed: Apr 2015)

[1.15] A. Jain et al.: *The Materials Project: A materials genome approach to accelerating materials innovation*: Applied Physics Letters Materials **1**, 011002 (2013)

[1.16] P. A. Rodnyi.: *Physical Processes in Inorganic Scintillators*: New York (CRC Press, 1997)

[1.17] H. v. Spijker.: *Luminescence and scintillation of Ce^{3+} doped materials for gamma-ray detection*: Netherlands (Delft University Press, 1999)

[1.18] E. Zych et al.: *Luminescence properties of Ce-activated YAG optical ceramic scintillator materials*: Journal of Luminescence **75** 193-203 (1997)

[1.19] D. A. Pawlak et al.: *Correlation between structural parameters of garnet and garnet-like structures*: Acta Crystallographica Section B **55** 736-744 (1999)

[1.20] T. Ishii et al.: *Theoretical calculation for the multiplet structure of the tetrahedrally coordinated Cr^{4+} in $Y_3Al_5O_{12}$*: Journal of Chemical Physics **115** 492-508 (2001)

[1.21] T. Ishii: *First-principles calculations for the cooperative transitions of Yb^{3+} dimer clusters in $Y_3Al_5O_{12}$ and Y_2O_3 crystals*: Journal of Chemical Physics **122** 024705 (2005)

[1.22] G. Pari et al.: *First-principles electronic structure calculations of $R_3Al_5O_{12}$ (R being the rare-earth elements Ce-Lu)*: Physica B **365** 163-172 (2005)

[1.23] N. J. Cherepy et al.: *Cerium-doped single crystal and transparent ceramic lutetium aluminum garnet scintillators*: Nuclear Instruments and Methods in Physics Research A **579** 38-41 (2007)

[1.24] E. Mihokova et al.: *Luminescence and scintillation properties of YAG:Ce single crystal and optical ceramics*: Journal of Luminescence **126** 77-80 (2007)

[1.25] C. R. Stanek et al.: *The effect of intrinsic defects on $RE_3Al_5O_{12}$ garnet scintillator performance*: Nuclear Instruments and Methods in Physics Research A **579** 27-30 (2007)

[1.26] T. Yanagida et al.: *Improvement of ceramic YAG(Ce) scintillators to $(YGd)_3Al_5O_{12}(Ce)$ for gamma-ray detectors*: Nuclear Instruments and Methods in Physics Research A **579** 23-26 (2007)

[1.27] J. Chen et al.: *Ab initio study of a charged vacancy in yttrium aluminum garnet*: Journal of Physics: Condensed Matter **20** (2008)

[1.28] A. Munoz-Garcia et al.: *First-Principles Study of the Structure anad the Electronic Structure of Yttrium Aluminum Garnet $Y_3Al_5O_{12}$*: International Journal of Quantum Chemistry **109** 1991-1998 (2009)

[1.29] A. Munoz-Garcia et al.: *Structural effects and 4f-5d transition shifts induced by La codoping in Ce-doped yttrium aluminum garnet: First-principless study*: Physical review B **82** 064114 (2010)

[1.30] A. Munoz-Garcia et al.: *Structural, electronic, and spectroscopic effects of Ga doping on Ce-doped yttrium aluminum garnet: First-principles study*: Physical review B **82** 183118 (2010)

[1.31] J. Saal et al.: *First-Principles Thermochemistry and Thermodynamic Modeling of the Al_2O_3-Nd_2O_3-SiO_2-Y_2O_3 Peudoquaternary System*: Journal of American Ceramic Society **93** 4158-4167 (2010)

[1.32] Z. Huang et al.: *First-principles calculations of structural and thermodynamic properties of $Y_3Al_5O_{12}$*: Solid State Communications **151** 1559-1563 (2011)

[1.33] A. Munoz-Garcia and L. Seijo: *Ce and La Single- and Double- Substitutional Defects in Yttrium Aluminum Garnet: First-Principles Study*: Journal of Physical Chemistry. A **115** 815-823 (2011)

[1.34] T. Yanagida et al.: *Scintillation properties of transparent ceramic and single crystalline Nd:YAG scintillators*: Nuclear Instruments and Methods in Physics Research A **631** 54-57 (2011)

[1.35] S. P. Feofilov et al.: *Mechanisms for Ce3+ excitation at energies below the zero-phonon line in YAG crystals and nanocrystals*: Journal of Luminescence **132** 3082-3088 (2012)

[1.36] H. Guo et al.: *First principles study of structural, phonon, optical, elastic and electronic properties of $Y_3Al_5O_{12}$*: Physica B **407** 2262-2266 (2012)

[1.37] S. Jiang et al.: *Correlation of the atomic and electronic structures and the optical properties of the Σ5(210)/[001] symmetric tilt grain boundary in yttrium aluminum garnet*: Acta Materialia **60** 7014-7050 (2012)

[1.38] Z. Li et al.: *Mechanism of Intrinsic Point Defects and Oxygen Diffusion in Yttrium Aluminum Garnet: First-principles Investigation:* Journal of American Ceramic Society **95** 3628-3633 (2012)

[1.39] O. Sidletskiy et al.: *Structure and scintillation yield of Ce-doped Al-Ga substituted yttrium garnet*: Materials Research Bulletin **47** 3249-3252 (2012)

[1.40] D. Solodovnikov et al.: *Single crystal Ce doped scintillator material with garnet structure sensitive to gamma ray and neutron radiation*: Journal of Crystal Growth **352** 99-102 (2012)

[1.41] X. Zhou et al.: *Luminescent properties and energy transfer of $Y_3Al_5O_{12}:Ce^{3+}$, Ln^{3+} (Ln=Tb, Pr) prepared by polymer-assisted sol-gel method*: Journal of Luminescence **132** 3004-3009 (2012)

[1.42] V. P. Dotsenko et al.: *Synthesis and luminescent study of Ce^{3+}-doped terbium-yttrium aluminum garnet*: Journal of Alloys and Compounds **550** 159-163 (2013)

[1.43] S. Jiang et al.: *Ab initio study the effects of Si and Mg dopants on point defects and Y diffusion in YAG*: Computational Materials Science **69** 261-266 (2013)

[1.44] J. Li et al.: *Densification and optical properties of transparent Ho:YAG ceramics*: Optical Materials **35** 748-752 (2013)

[1.45] J. M. Ogieglo et al.: *Luminescence and energy transfer in $Lu_3Al_5O_{12}$ scintillators co-doped with Ce^{3+} and Pr^{3+}*: Optical Materials **35** 322-331 (2013)

[1.46] T. Zhao et al.: *Effects of Ho^{3+}-doping concentration on the performances of resonantly pumped Ho:YAG ceramic lasers*: Optical Materials **35** 712-714 (2013)

[1.47] Yu. Zorenko et al.: *Multi-component Ce doped $(Gd,Y,La,Lu)_3(AlGaSc)_5O_{12}$ garnets – A new story in the development of scintillating single crystalline film screens*: Radiation Measurements **56** 150-154 (2013)

[1.48] Y. Zou et al.: *High-effciency diode-pumped Tm:YAG ceramic laser*: Optical Materials **35** 804-806 (2013)

[1.49] N.A. Azarenkov et al.: *Ion-photon emission under ion bombardment of garnet structures of different composition*: Vacuum **105** 91-95 (2014)

[1.50] Z. Huang et al.: *Antisite defect in nonstoichiometric yttrium aluminum garnet: Experimental and first-principles calculation*: Journal of European Ceramic Society **34** 783-790 (2014)

[1.51] J. A. Mares et al.: *Cerium-doped $RE^{3+}AlO_3$ perovskite scintillators: Spectroscopy and radiation induced defects*: Journal of Alloys and Compounds **275-277** 200-204 (1998)

[1.52] A.J. Wojtowicz et al.: *Thermoluminescence and Scintillation of $LuAlO_3$:Ce* : Radiation Materials **29** 323-326 (1998)

[1.53] A.J. Wojtowicz et al.: *Electron traps and scintillation mechanism in $YAlO_3$:Ce and $LuAlO_3$:Ce scintillators*: Journal of Luminescence **79** 275-291 (1998)

[1.54] A.G. Petrosyan et al.: *Bridgman single crystal growth of Ce-doped $(Lu_{1-x}Y_x)AlO_3$* : Journal of Crystal Growth **198/199** 492-496 (1999)

[1.55] J. Chval et al.: *Development of new mixed $Lu_x(RE^{3+})_{1-x}AP$:Ce scintillators ($RE^{3+}=Y^{3+}$ or Gd^{3+}): comparison with other Ce-doped or intrinsic scintillating crystals*: Nuclear Measurements and Methods in Physics Research A **443** 331-341 (2000)

[1.56] J. Glodo, A.J. Wojtowicz: *Thermoluminescence and scintillation properties of LuAP and YAP*: Journal of Alloys and Compounds **300-301** 289-294 (2000)

[1.57] J. A. Mares : *Spectroscopy and characterization of Ce^{3+}-doped pure or mixed $Lu_x(RE^{3+})_{1-x}AlO_3$ scintillators*: Journal of Alloys and Compounds **300-301** 95-100 (2000)

[1.58] D. M. Bercha et al.: *Elementary energy bands in ab intitio calculations of the $YAlO_3$ and SbSI crystal band structure*: Physical review B **66**, 195203 (2002)

[1.59] C. Kuntner et al.: *Scintillation properties and mechanism in Lu0.8Y0.2AlO3:Ce*: Nuclear Instruments and Physics Research A **486** 176-180 (2002)

[1.60] C. Kuntner et al.: *Intrinsic energy resolution and light output of the $Lu_{0.7}Y_{0.3}AP$:Ce scintillator*: Nuclear Instruments and Methods in Physics Research A **493** 131-136 (2002)

[1.61] J. A. Mares et al.: *Growth and properties of Ce^{3+} doped $Lu_x(RE^{3+})_{1-x}AP$ scintillators*: Optical Materials **19** 117-122 (2002)

[1.62] M. Nikl et al.: *An effect of Zr^{4+} co-doping of YAP:Ce scintillator*: Nuclear Instruments and Methods in Physics Research A **486** 250-253 (2002)

[1.63] J.A. Mares et al.: *Scintillation and spectroscopic properties of Ce^{3+}-doped $YAlO_3$ and $Lu_x(RE)_{1-x}AlO_3$ ($RE=Y^{3+}$ and Gd^{3+}) scintillators*: Nuclear Instruments and Methods in Physics Research A **498** 312-327 (2003)

[1.64] S. Belogurov et al.: *Properties of Yb-doped scintillators: YAG, YAP, LuAG*: Nuclear Instruments and Methods in Physics Research A **516** 58-67 (2004)

[1.65] A. Krasnikov et al.: *Luminescence and defects creation in Ce^{3+}-doped aluminium and lutetium perovskites and garnets*: Nuclear Instruments and Methods in Physics Research A **537** 130-133 (2005)

[1.66] C. Kuntner et al.: *Advances in the scintillation performances of LuYAP:Ce single crystals*: Nuclear Instruments and Methods in Physics Research A **537** 295-301 (2005)

[1.67] J. A. Mares et al.: *Ce^{3+}-doped scintillators: status and properties of (Y, Lu) aluminium perovskites and garnets*: Nuclear Instruments and Methods in Physics Research A **537** 271-275 (2005)

[1.68] W. Drozdowski et al.: *Scintillation properties of LuAP and LuYAP crystals activated with Cerium and Molybdenum*: Nuclear Instruments and Methods in Physics Research A **562** 254-261 (2006)

[1.69] A.G. Petrosyan et al.: *Properties of LuAP:Ce scintillator containing intentional impurities*: Nuclear Instruments and Methods in Physics Research A **571** 325-328 (2007)

[1.70] Y. Zorenko et al.: *Peculiarities of luminescence and scintillation properties of YAP:Ce and LuAP:Ce single crystals and single crystalline films*: Radiation Measurements **42** 528-532 (2007)

[1.71] M. Zhuravleva et al.: *Crystal Growth and scintillation properties of Pr-doped YAlO3*: Optical materials **30** 171-173 (2007)

[1.72] M. Zhuravleva et al.: *Crystal Growth and scintillation properties of $YAlO_3$:Pr co-doped with Mo^{3+} and Ga^{3+} ions*: Journal of Crystal Growth **311** 537-540 (2009)

[1.73] T.B. de Queiroz et al.: *Luminescence characteristics of YAP:Ce scintillator powder and composites*: Optical materials **32** 1480-1484 (2010)

[1.74] T. Yanagida et al.: *Growth and scintillation properties of Pr doped YAP with different Pr concentrations*: Nuclear Instruments and Methods in Physics Research A **623** 1020-1023 (2010)

[1.75] A. Phunpueok et al.: *Scintillation response of YAlO3:Ce and $Lu_{0.7}Y_{0.3}AlO_3$:Ce single crystal scintillators*: Nuclear Instruments and Methods in Physics Research B **286** 76-79 (2012)

[1.76] D. Totsuka et al.: *Crystal growth and characterization of Tm doped mixed rare-earth aluminum perovskite*: Materials Research Bulletin **47** 993-997 (2012)

[1.77] M. Zhuravleva et al.: *Crystal Growth and scintillation properties of $YAlO_3$:Pr co-doped with Mo^{3+} and Ga^{3+} ions*: Journal of Crystal Growth **311** 537-540 (2009)

CHAPTER 2

THEORY: THE BACKGROUND OF DENSITY FUNCTIONAL THEORY

2.1. What is Density Functional Theory?

Density-functional theory is the most widely used and the most successful way to solve Schrodinger equation of the electron structure of matter [2.1]. In the original formulation of DFT, it provides the ground state property of a system where the electron density plays a crucial role. The original DFT has been generalized to be suitable in many different situations; nowadays it is routinely applied in many different fields including fields that were thought to be more distant from quantum mechanical calculations such as biology and mineralogy. The wide application of DFT can also include atoms, molecules, solids, nuclei, both quantum and classical fluids and more [2.2].

The versatility of DFT comes from the generality of its core concepts and the flexibility of implementation. Despite the generality and the flexibility, the DFT is based on a solid conceptual framework. In this chapter the framework will be introduced in general terms along with two core elements within it, the Hohenberg-Kohn theorem and the Kohn-Sham equations and the approximations that make the DFT calculations practical.

To begin explaining what density-functional theory is, it is helpful to go back to some elementary quantum mechanics. In quantum mechanics it is stated that all the information that one can possibly know about a system can be extracted from the system's wave function, Ψ. Especially, the focus will be on the wave functions of electronic structures of atoms, molecules and solids. In the case of crystal lattice in a solid, the wave function depends only on the

coordinates of the electrons since the nuclear degrees of freedom exist only as a potential $\boldsymbol{v(r)}$ influencing the electrons. Since electrons are assumed to be moving in nonrelativistic speed here, this electron wave function can be calculated from the nonrelativistic Schrodinger equation for a single electron moving under influence of a potential function $\boldsymbol{v(r)}$ is

$$\left[-\frac{\hbar^2\nabla^2}{2m}+v(r)\right]+\Psi(r)=\epsilon\Psi(r) \tag{2.1}$$

If it is a many-body problem the Schrodinger equation becomes

$$\left[\sum_i^N\left(-\frac{\hbar^2\nabla_i^2}{2m}+v(r_i)\right)+\sum_{i<j}U(r_i,r_j)\right]\Psi(r_1,r_2\ldots,r_N)=E\Psi(r_1,r_2\ldots,r_N) \tag{2.2}$$

with N representing the number of electrons and $U(r_i,r_j)$ representing the electron-electron interaction. The electron-electron interaction operator for the Coulomb system, the only system that is considered in this thesis, is

$$\hat{U}=\sum_{i<j}U(r_i,r_j)=\sum_{i<j}\frac{q^2}{|r_i-r_j|} \tag{2.3}$$

This interaction operator is the same operator that appears in any system with Coulomb interactions between particles. Similar applies to the kinetic energy operator

$$\hat{T}=-\frac{\hbar^2}{2m}\sum_i\nabla_i^2 \tag{2.4}$$

which is the same in any nonrelativistic system. Any system ranging from a single atom system to a solid system the dependence is only on the potential $\boldsymbol{\upsilon(r_i)}$ **.** In case of a system with a single atom

$$\hat{V}=\sum_i v(r_i)=\sum_i\frac{Qq}{|r_i-R|'} \tag{2.5}$$

where Q represents the charge of the nucleus and R is the position of the nucleus. Q can also be expressed as the product of Z and e where Z is the atomic number and e is the positive elementary charge. For a single atom system R is usually taken to be the origin of the coordinate system so that it can be taken out from the equation. For a molecule or a solid system the above equation becomes

$$\widehat{\boldsymbol{V}} = \sum_{\boldsymbol{i}} \boldsymbol{v}(\boldsymbol{r_i}) = \sum_{\boldsymbol{ik}} \frac{\boldsymbol{Q_k q}}{|\boldsymbol{r_i} - \boldsymbol{R_k}|'} \tag{2.6}$$

where the sum on the index k runs over all nuclei of the system. Each nucleus has a charge of $Q_k = Z_k e$ and position R_k. The only factors that fundamentally distinguish a molecule from a solid are the spatial arrangements of the R_k along with corresponding boundary conditions. On a similar note, only the difference in the $\hat{U}$ term is what distinguishes a simple single-body quantum mechanics problem of equation (2.1) from the extremely complex N-body problem of equation (2.2). Density-functional theory has these properties built into it in a very fundamental way [2.1].

DFT is a very versatile alternative way of many computationally demanding methods to for solving many-body Schrodinger's equation. DFT takes the advantage of the fact in nonrelativistic Coulomb systems it is only the potential $\boldsymbol{v}(\boldsymbol{r})$ that differs hence dealing with $\hat{U}$ and $\hat{T}$ once and for all. Also, DFT enables to systematically map a many-body system onto a single-body problem meaning mapping a system with $\hat{U}$ onto a system without $\hat{U}$. This process is made possible by taking the particle density n(r) to be the key variable among many other observables and using this n(r) to calculate all other observables. In the following sections, conceptual structures of DFT and other forms it takes in applications are explained.

2.2. The Hohenberg-Kohn theorem

Two mathematical theorems proved by Hohenberg and Kohn are at the heart of DFT. The first Hohenberg-Kohn theorem states: *The ground-state energy from Schrodinger's equation is a unique functional of the electron density* [2.3].

Meaning that there exists a one-to-one mapping between the ground-state wave function and the ground state electron density [2.4]. It can also be stated as the ground-state electron density uniquely determines all properties (including energy and wave function of ground state). This implies that the Schrodinger's equation can be solved by finding a function of three spatial variables (the electron density) instead of 3N variables. Despite of the intensive proof of the Hohenburg-Kohn theorem, unfortunately it only states that there exists an electron density functional but not stating anything about what the functional actually is.

The second Hohenberg-Kohn theorem states an important property of the electron density functional: *The electron density that minimizes the energy of the overall functional is the true electron density corresponding to the full solution of the Schrodinger equation* [2.3]. Meaning that given this true functional form is known, the electron density could be varied until the energy of the overall functional get minimized hence enabling one to find the associated electron density. The second Hohenberg-Kohn theorem is also called the variational principle and it is practical with approximation of the functional.

This energy functional in the Hohenberg-Kohn theorem can be written down in terms of the wave function of a single electron, $\psi_i(r)$. Keeping in mind that the density of electrons $n(r)$ can be defined from these single-electron wave functions.

$$\boldsymbol{n(r) = 2\sum_{i} \psi_i^*(r)\psi_i(r)} \tag{2.7}$$

The energy functional can be expressed as

$$\boldsymbol{E}[\{\boldsymbol{\psi_i}\}] = \boldsymbol{E_{known}}[\{\boldsymbol{\psi_i}\}] + \boldsymbol{E_{XC}}[\{\boldsymbol{\psi_i}\}] \tag{2.8}$$

where the functional is taken into parts. $\boldsymbol{E_{known}}[\{\boldsymbol{\psi_i}\}]$ as a collection of terms that can be written down as a simple analytical form and everything else in E_{XC} term. The E_{known} term has four parts

$$\boldsymbol{E_{known}}[\{\boldsymbol{\psi_i}\}] = \frac{\boldsymbol{h^2}}{\boldsymbol{m}}\sum_i \int \boldsymbol{\psi_i^*}\boldsymbol{\nabla^2}\boldsymbol{\psi_i}\boldsymbol{d^3}\mathbf{r} + \int \boldsymbol{V}(\boldsymbol{r})\boldsymbol{n}(\boldsymbol{r})\boldsymbol{d^3}\boldsymbol{r}$$

$$+\frac{\boldsymbol{e^2}}{\boldsymbol{2}}\int\int \frac{\boldsymbol{n}(\boldsymbol{r})\boldsymbol{n}(\boldsymbol{r'})}{|\boldsymbol{r}-\boldsymbol{r'}|}\boldsymbol{d^3}\boldsymbol{r}\boldsymbol{d^3}\mathbf{r'} + \boldsymbol{E_{ion}} \tag{2.9}$$

The four contributing terms are the kinetic energies of the electrons, the nuclei-electron Coulomb interaction, the Coulomb interaction between electrons and the Coulomb interaction between nuclei. The other term, $\boldsymbol{E_{XC}}[\{\boldsymbol{\psi_i}\}]$, accounts for the exchange-correlation functional, and it includes the rest of the quantum mechanical effects that are left out from the known term.

2.3. Kohn-Sham Equation

Setting the exchange-correlation energy functional aside, so far minimizing the energy of the total energy functional is not any easier than solving the Schrodinger equation for the waves function. The Kohn-Sham equations help reducing down the difficulty by solving a non-interacting Schrodinger equation instead of solving the many-body Schrodinger equation to find the correct election density. The Kohn-Sham equations are expressed as [2.5]

$$\left[\frac{\boldsymbol{h^2}}{\boldsymbol{2m}}\boldsymbol{\nabla^2} + \boldsymbol{V}(\boldsymbol{r}) + \boldsymbol{V_H}(\boldsymbol{r}) + \boldsymbol{V_{XC}}(\boldsymbol{r})\right]\boldsymbol{\psi_i}(\boldsymbol{r}) = \boldsymbol{\varepsilon_i}\boldsymbol{\psi_i}(\boldsymbol{r}) \tag{2.10}$$

The equation is similar looking to equation (1.2) but the important difference is that the summations that were inside the full Schrodinger equation are absent. The summations are

missing because the solution to the Kohn-Sham equations are single-electron wave function, $\boldsymbol{\psi_i(r)}$, that only depends on the three spatial variables. V, V_H and V_{XC} on the left side of the KS equations are the three potentials. The first potential V appears in both in the full Schrodinger equation, equation (1.2) and in equation (2.9). This potential represents the interaction between one electron and the group of atomic nuclei. The second potential V_H is known as the Hartree potential. V_H is defined as

$$\boldsymbol{V_H}(\mathbf{r}) = \boldsymbol{e^2} \int \frac{\boldsymbol{n(r')}}{\boldsymbol{|r - r'|}} \boldsymbol{d^3 r'} \tag{2.11}$$

This Hartree potential accounts for the Coulomb repulsion between the total electron density characterized by all the electrons in the system and the electron being represented in one of the Kohn-Sham equations. The Hartree potential includes the interaction with an electron that is considered in one of the Kohn-Sham equation and the same electron as a part of the total electron density. This unphysical self-interaction part is included in the Hartree potential; however, the correction for this self-interaction is in the third potential, V_{XC}. V_{XC} can be described as the functional derivative of E_{XC}

$$\boldsymbol{V_{XC}}(\mathbf{r}) = \frac{\boldsymbol{\delta E_{XC}(r)}}{\boldsymbol{\delta n(r)}} \tag{2.12}$$

Although functional derivative harder to analyze than derivative of a function here one can conceptually think of it as a regular derivate.

With the Kohn-Sham equations defined above the solution the algorithm to solve for the ground-state electron density is to start with a guessed trial electron density, *n(r)*. Using the initial electron density solve the KS equations to find the wave functions of a single particle, $\boldsymbol{\psi_i(r)}$. Find the electron density by substituting $\boldsymbol{\psi_i(r)}$into the equation

$$\boldsymbol{n_{KS}}(\mathbf{r}) = \mathbf{2} \sum_i \boldsymbol{\psi_i^*(r)\psi_i(r)} \tag{2.13}$$

Compare the resultant $n_{KS}(r)$ from equation (2.13) with *n(r)* which is the electron density that was used to solve the KS equation. If they are the same then *n(r)* is the ground-state density which then can be used to calculate the total energy of the system. If $n_{KS}(r)$ and *n(r)* are different the algorithm has to be re-run with an updated *n(r)*. Eventually with successful updating of *n(r)* the algorithm will result in a self-consistent solution of KS equations.

2.4. Exchange-Correlation Functional

Now $\boldsymbol{E_{XC}}[\{\boldsymbol{\psi_i}\}]$ term from equation (2.8) needs to be defined to complete the puzzle. However, it is very difficult to define the $\boldsymbol{E_{XC}}[\{\boldsymbol{\psi_i}\}]$, in fact even though the existence of the exchange-correlation functional was guaranteed by the Hohenberg-Kohn theorem the true form of the functional is simply not known. Nevertheless, in the special case of uniform electron gas system the functional can be worked out exactly. This *n(r)* = constant situation might not look so interesting and not so useful but it serves as a practical case to actually use the KS equations. In order to proceed with the calculation at each position the exchange-correlation potential has to be set with known value from the uniform electron gas system at the density of electron observed at that position

$$\boldsymbol{V_{XC}}(\mathbf{r}) = \boldsymbol{V_{XC}^{electron\ gas}}[\boldsymbol{n}(\boldsymbol{r})] \tag{2.14}$$

Since this approximation defines the exchange-correlation functional by using only the local density it is called the local density approximation (LDA). With LDA one can completely define the KS equations; however, these equations are not the exact solution for the true Schrodinger equation since true exchange-correlation functional is not in use. Apart from LDA there is another approximation called generalized gradient approximation (GGA) where it uses

the information on the local gradient in the density of electron along with the local electron density itself. At a first glance it might seem like GGA is more accurate than LDA since it contains more information but that is not always the case. Since there are several different ways to include information from the gradient of the density of the electron to a GGA functional there are many distinct GGA functionals. Perdew-Wang functional (or PW91) and Perdew-Burke-Ernzerhof(or PBE) functional to name a couple of them. There are many other GGA functionals and each of them will give somewhat different results hence one needs to be specify along with the result which approximations were used for the DFT calculation.

2.5. Approximation Method

The most popular approximation for the exchange-correlation functional is the local-density approximation that was introduced by Kohn and Sham at the same time the KS equations were introduced. With local density approximation (LDA) the exchange correlation functional E_{XC} can be calculated assuming that the exchange-correlation energy has the same energy as a uniform electrons gas system with density $\rho = \rho(r)$ for each infinitesimal increment of density $\rho(r)\, dr$. Then E_{XC} is given as

$$\boldsymbol{E_{XC}} = \int \boldsymbol{dr\rho(r)\epsilon_{XC}(\rho(r))} \tag{2.15}$$

where $\boldsymbol{\epsilon_{XC}(\rho(r))}$ presents each electron's exchange-correlation energy in a uniform density electron system with density ρ [2.6]. LDA is not actually correct because near the atoms the charge density is definitely not uniform. However, the uniform electron gas system is the only system that E_{XC} can be calculated and hence the only system to construct $\boldsymbol{\epsilon_{XC}(\rho(r))}$ on. LDA seems wrong, nonetheless, it works. The justification is a very hind-sighted one with thousands

of working applications which proves that it can accurately provide simulated properties of materials. However, for some cases LDA does perform poorly and it is due to the fact that spatial variation of the density is ignored. Another approximation method called generalized-gradient approximation (GGA) was developed to account for this dependence on this gradient of the density. In GGA predicted binding and dissociation energies are improved. That is why GGA method has been chosen to simulate the properties of the materials in this work.

One of the most prominent ways of DFT calculation was developed by Roberto Car and Michele Parrinello. It did not introduce any new theories or fundamental methods but they pointed out the key elements to make effective DFT calculations. There are five main features of the Car-Parrinello approach. Car-Parrinello approach represents the wavefunction with a plane-wave basis to and replaces the ionic cores with pseudopotentials. It uses fast-Fourier transforms and minimizes the total energy to get to the ground state. For molecular dynamics it uses fictitious dynamics of the electrons within a unified Lagrangian formalism. All of them do not need to be used at the same time as in the case of conjugate-gradient approach by Mike Payne embedded in the CASTEP code. The method used in CASTEP code includes planes waves, pseudopotentials and fast Fourier transforms.

2.6. Plane-wave Pseudopotential

Plane waves and pseudopotentials are the critical part of the DFT calculation method. They are very fundamental and their advantages and disadvantages need to be looked at. In the plane-wave pseudopotential (PWP) method the system is simulated as a 3D supercell with periodicity which enables Bloch's theorem to be used to the electron wavefunctions [2.6].

$$\boldsymbol{\psi_{n,k}(r) = u_{n,k}(r)\exp(ik \cdot r)} \tag{2.16}$$

The periodicity of the supercell is described by the function $u(r)$. Many other mathematical forms are possible but the usual choice is the series expansion expressed with a set of basis functions. For PWP method, plane waves are used as the basis functions so each single electron wavefunction $\psi_{n,k}$ is described as

$$\boldsymbol{\psi_{n,k}(r) = \sum_{G} u_{n,k}(G) exp(i(k + G) \cdot r)} \tag{2.17}$$

with expansion coefficients $u_{n,k}$. The wavevectors G are chosen so that the plane waves and the supercell are commensurate. In principle, the number of G-vectors and the number of k's should be infinite. The exponential term represents a plane wave with wavevector k and it has to be commensurate with the whole system not just the periodically repeated cell. There exist an infinite number of k vectors with the solutions for each $\psi_{n,k}$ in an infinite system. These infinite k vectors simply indicates that there is infinite number of electrons; however, they system is greatly simplified when it is realized that for close k-points the change in $\psi_{n,k}$ is negligible. This is simplifies the calculation significantly because only a finite number of k-points are needed. This is also known as the k-point sampling. Also an infinite number of wavevectors G are needed for exact wavefunction representation but it is not necessary because summation of a finite wavevectors G will give sufficiently accurate representation of the wavefunction.

The advantages of the plane-wave basis are it is unbiased hence all the space is treated the same. It is complete which mathematically means that the linear combination of the basis spans all space. There is one convergence criterion. Mathematically plane waves are simple to deal with, do not depend on the atomic positions and their derivatives are products in k-space. However there are some disadvantages as always. The biggest curvature of the wavefunction

defines the necessary number of plane waves. Empty spaces costs as much as the area of interest to calculate.

The fact that it is unbiased, complete and it has a single convergence criterion means that it can always be ensured if the basis set if suitable for the calculation. One simply needs to stop increasing the number of plane waves when the quantity of interest does not change anymore. Particularly, the largest wavevector in the plane-wave basis determines the quality of the basis set and this parameter is usually expressed in terms of energy. This energy is the energy of a free electron with wavefunction that has the matching wavevector as the largest wavevector of the plane-wave basis set.

$$\boldsymbol{E_c} = \frac{\hbar^2(\mathbf{G}+\mathbf{k})^2}{2\boldsymbol{m}} \tag{2.18}$$

All plane waves that have wavevectors of wavefunctions of electrons that have less than the cutoff energy E_c are used for the expansion. This is very valuable since plane waves are mathematically simple so the method implementation is easier, especially for the ionic forces calculation which adds little cost to the calculation. Also the originless property of plane waves is important. The plane waves are independent of the atomic positions and forces are again independent of the basis set. Furthermore, additional developments are easiest with plane-wave codes.

2.7. Pseudopotentials

The fact that the biggest curvature of the wavefunction defines the necessary number of plane waves is a serious disadvantage of plane-wave basis computation wise. In condensed matter how the valence electrons behave is the main interest and free-electron picture is not far off from the valence states. However, this is not the case for the valence wavefunction near the atomic cores. Near the atomic cores the valence wavefunction changes drastically because of the strong Coulomb potential. It is even worse for the localized and tightly bounded core electron states. A very large number of planes waves would be needed to for accurate representation of electronic wavefunctions, however, by using both pseudopotentials and fast Fourier transform (FFT) this problem can be overcome. Pseudopotential method removes the nucleus of the atom and the core electrons around it from the picture and instead replaces it with a fixed effective potential. More importantly, the pseudopotential can be taken as a weaker potential than what it actually is hence reducing the curvature of the wavefunction in the nucleus region which again reduces the number of planes waves needed. This also reduces the number of electrons to be calculated because electrons in the core area have been removed. FFT offers an efficient way to transform the wavefunction and the charge density from the real space to the reciprocal space and vice versa. This ease of transformation is an advantage because for different parts of the calculation one space is cheaper to perform the calculation over the other hence the calculation can always be done in the easier one.

There are two valid reasons for using the pseudopotential. The first one is that the wavefunctions near the nucleus of an atom not important as far as the bonding are concerned. It is the bonding that decides most of the properties of the materials hence the full details for

those wavefunctions near the nucleus are not needed. The second one is that it is most often times correct to assume that the core orbitals are not affected by the environment that they are in. The idea of transferability is crucial in the construction of pseudopotentials.

Modern pseudopotentials are built using first principles. The key is to substitute the real potential that results from the charge of the nucleus and the core electrons, with an effective potential that encompasses the core region with a chosen radius r_c. However, this effective potential has some requirements to be met. It must have the same valence orbital eigenvalues as the all-electron calculation of the system. Both the continuity of the wavefunctions and the first derivatives of the wavefunctions have to be preserved across the core boundary. For the last requirement the charge integration within the core radius r_c has to yield the same result for the real potential system and the effective potential system, in other words, the pseudopotential has to be norm-conserving. When all these requirements are met, then the pseudopotential gives the same scattering properties with energies of the valence eigenvalues as the real ionic core that was replaced. The norm conservation also guarantees that the electrostatics is approximately right outside the core region.

However, there are still a couple of drawbacks to the pseudopotential. First it is hard to decide which valence electronic configuration has to be used. It would be ideal if the pseudopotential was transferrable completely then the configuration would not matter but for some elements a neutral atom and an ionized atom gives very different pseudopotential. Related to this, it is also difficult to decide which electrons can be defined to be core electrons because sometimes the overlap of the core states and valence states are blurred thus making it hard to distinguish. Another drawback is that one can never be sure if the pseudopotentials valence eigenvalues exactly matches the all electron eigenvalues throughout the entire valence

band energy range. This means that pseudopotential calculated from a single atom is still an approximation even in the best cases.

2.8. Ultrasoft Pseudopotential

Although pseudopotential works most of the times, norm-conserving pseudopotentials demands very large number of plane waves and high value of E_c. To address this issue Vanderbilt proposed to relax the norm-conservation requirement to generate ultrasoft pseudopotential which allows fewer plane waves for a desired accuracy [2.7]. The charges within pseudopotential radius results from hard augmentation function and valence charges result from soft augmentation function. The accuracy on the scattering properties is somewhat lost due to the relaxation of the norm-conserving requirement; however, for compensation pseudopotential uses two or three reference energies as guide. Ultrasoft pseudopotential seem to have much better transferability than the norm-conserving, in fact, a mere neutral atom picture is enough to generate ultrasoft pseudopotentials. E_c value for the ultrasoft pseudopotential is typically half of the norm-conversing pseudopotential one and the number of plane waves required is about a one-third only.

References

[2.1] C. Klaus: *A bird's-eye view of density-functional theory*: Brazilian Journal of Physics **36** 1318-1343 (2006)

[2.2] J. C. Cuevas: *Introduction to density functional theory*: (https://www.uam.es/personal_pdi/ciencias/jcuevas/Talks/JC-Cuevas-DFT.pdf) (2004) (Apr 2015)

[2.3] P. Hohenberg and W. Kohn: *Inhomogeneous electron gas*: Physical Review **136** B864 (1964)

[2.4] D. Sholl and JA. Steckel: *Density Functional Theory: A practical introduction* (Wiley, 2009)

[2.5] W. Kohn and L. J. Sham: *Self-consistent equations including exchange and correlation effects*: Physical Review **140** A1133 (1965)

[2.6] M. D. Segall: *First-principles simulation: ideas, illustrations and the CASTEP code*: Journal of Physics **14** 2717 (2002)

[2.7] D. Vanderbilt: *Soft self-consistent pseudopotentials in a generalized eigenvalue formalism*: Physical Review B. **41** 7892 (1990)

CHAPTER 3

METHOD: CASTEP SOFTWARE

3.1. CASTEP Background

3.1.1. Introduction

CASTEP (Cambridge Sequential Total Energy Package) program is a code to perform electronic structure calculation hence calculating properties of materials from quantum mechanical first principles. By using density functional theory CASTEP can simulate variety of materials including atoms, molecules, crystalline solids, liquids, surfaces or even amorphous materials. Basically, properties of any materials with an assembly of nuclei and electrons can be run in CASTEP as long as the computational resources permits. The aim of this simulation approach is use quantum mechanics instead of using empirical experimental data [3.1].

CASTEP was originally written in the late 1980's by Payne and his co-workers. It quickly gained its popularity in the community and new technologies and developments were contributed by researchers.

3.1.2. Background

As discussed in previous sections, solving many-body Schrodinger equation is a very difficult task so density functional theory is used to calculate the ground state energy electron structure of the system. Basic methodology implemented in CASTEP to calculate the electronic structure first starts with solving a set of single electron Schrodinger equations (or Kohn-Sham equations) with plane-wave pseudopotential approach. Using a plane waves basis

set the wavefunctions are expanded under periodic boundary conditions with Block's theorem. *ab initio* pseudopotentials describe the electron-ion potential using norm-conserving and ultrasoft formulations. From direct energy minimization scheme the electron wavefunctions and the relevant electron density function are found. Density mixing and conjugate gradient schemes are implemented and robust electron ensemble DFT approach can be used for partial occupancies system.

3.1.3. Capabilities

CASTEP is a first principle code that is fully featured with many capabilities. From first principles CASTEP aims to calculate the physical properties of the system, total energy being the basic quantity which can be used to derive other quantities. CASTEP uses *freeform* file format which means only some specific commands are needed for CASTEP to perform a calculation. All of the input variables have built-in default values including intelligent values for essential parameters like the plane wave cut off energy, Fourier transform and *k*-point sets and more. Running the code using command line is simple. As the calculation proceeds summary of the calculation is given off in an output file and calculation including charge densities and wavefunction coefficients are given off in a binary formatted file. The user can choose the run the code in either serial or parallel. If the user chooses to run the code in parallel then number of nodes selected in the input and a smart default parallel approach is selected depending on the number of processors and *k*-points. Graphic user interface of CASTEP is also available in a package called Material Studio from Accelrys. In Material Studio, one can build the initial crystallographic system, create input files, run calculations and analyze the result of the calculation. Total energy of the system is first calculated as a result of geometry

optimization to derive all other physical properties. Electronic structure output is of interest for this thesis which gives the band structure, total and partial density of states (DOS). CASTEP can also calculate physical properties like geometry of the structure, molecular dynamics, transition states, phonon information, electric field response and approximation of the exchange and correlation functional.

3.1.4. Example

With Material Studio one can build a crystal structure with desired space group, internal coordinates and lattice parameters using graphic user interface. The first step to build the desired structure is to build the lattice. Figure 3.1 below shows the build crystal dialog from Material Studio [3.2].

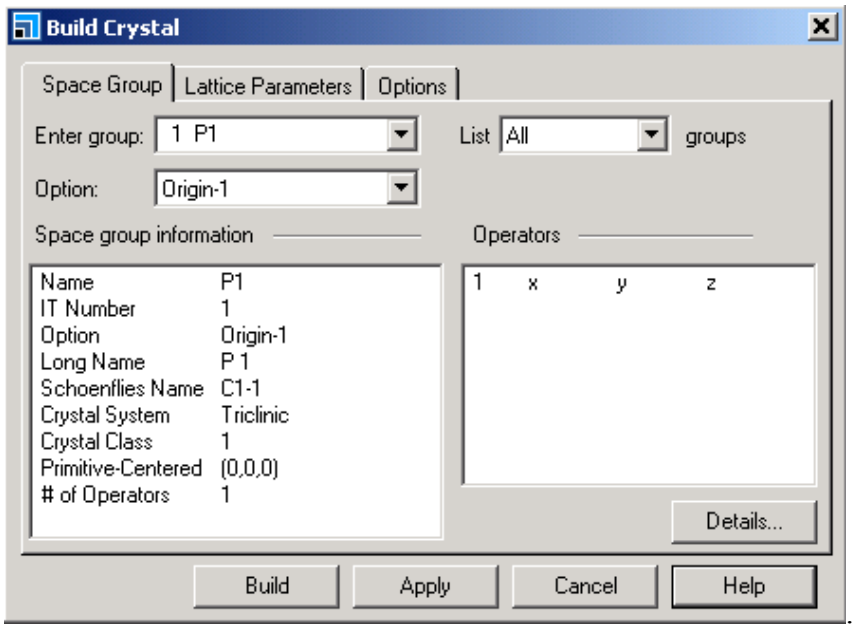

Figure 3.1. Build crystal dialog in Material Studio

The space group and the lattice parameters are specified in the relevant tabs in the dialog window. Atoms can be added into the empty lattice by using the add atoms dialog shown below selected from the build menu

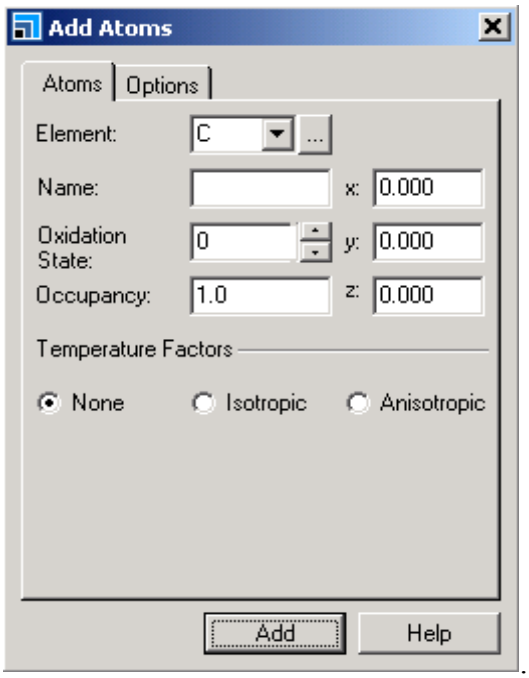

Figure 3.2. Add atoms dialog

Atoms can be added in with the choice of fractional coordinate system or Cartesian coordinate system. In the display style dialog numerous display style options are available including the balls and stick option which is the most commonly used. Balls and stick display style of a primitive cell of an example AlAs crystal is shown below

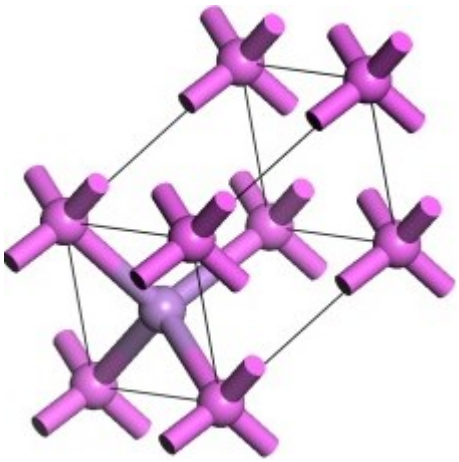

Figure 3.3. Primitive cell of an example AlAs crystal

Now a CASTEP calculation is ready to be run with the crystal structure that is created. From the modules toolbar CASTEP calculation dialog can be opened

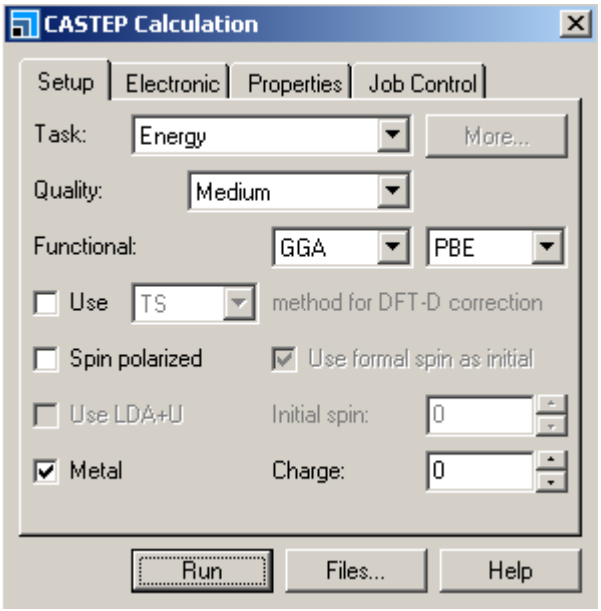

Figure 3.4. CASTEP calculation dialog

In the setup tab there are many calculations that can be done including energy, geometry optimization, dynamics, elastic constants and etc., with specified quality and approximation methods. From the properties tab one can specify which properties are also to

be calculated with options including band structure, density of states, optical properties and etc. In the case of band structure the Brillouin zone path of the calculation can be customized. In the job control tab the user can specify the options related to how the calculation is ran, for example, running the calculation from a remote server, update intervals, number of cores used for the calculations and more. After choosing all the desired options on all the tabs of the CASTEP window the calculation can be started.

When the calculation starts a set of progress files that contain all the progress of the calculation will be created which can be seen in the project explorer that deals with all the files that are relevant to the calculation. Each of these new files contains information about the calculation such as the convergence in energy, the total energy, stress, forces and the number of iterations. While the calculation is running the status can be monitored from a window called the job explorer. The job explorer shows active or terminated jobs with job identification numbers and the server information. The job can also be stopped or resumed in the job explorer. After the calculation has been completed, output files are created including the files with extensions *.xsd, .castep* and *.param*. The *.xsd* file has the 3D view of the final optimized structure, the *.castep* file is a text document that contains the optimization information and the *.param* file shows the input information of the calculation. From the *.xsd* file and the properties that are obtained from the job the CASTEP analysis can be run to show the result in a graphical format. Any plot of the resultant density of states, partial density of states, band structure or phonon dispersion can be done but here the partial density of states was chosen to be shown as an example.

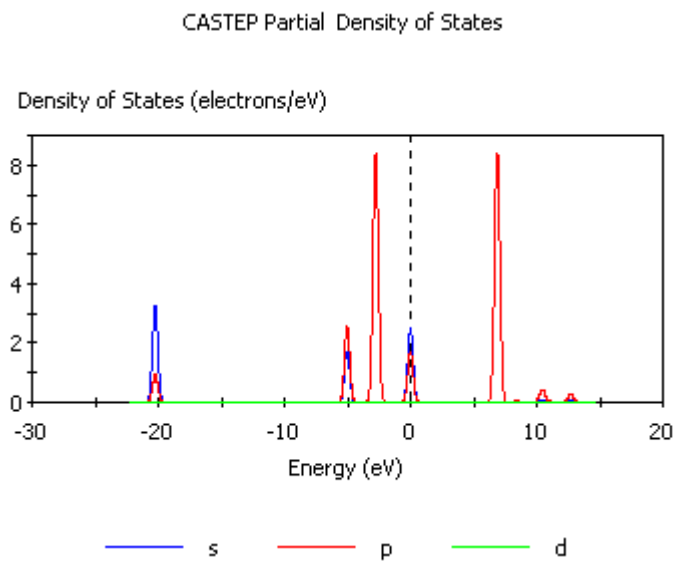

Figure 3.5 Partial density of states of an example CO molecule

Figure 3.6 shows the flowchart of a CASTEP calculation. It shows the steps that are involved in a calculation and in which order the calculation steps are performed in. The first three steps refer to the input from the user before the calculation is started and the rest steps are done within the program during the calculation. First the user has to create a new empty 3D atomistic document. Then the user creates a lattice structure in the atomistic document by specifying the space group and the lattice parameters. Atoms with specified coordinates are inserted into the lattice structure. In the fourth step, the program reads the atomic configuration created by the user. The program initiates the calculation by constructing initial electron density, potential, orbitals and pseudopotential. Then the Self Consistent Field (SCF) loop which is the main part of the calculation starts. When the SCF loop converges the calculation ends and results are printed on output files.

Flowchart of a CASTEP calculation

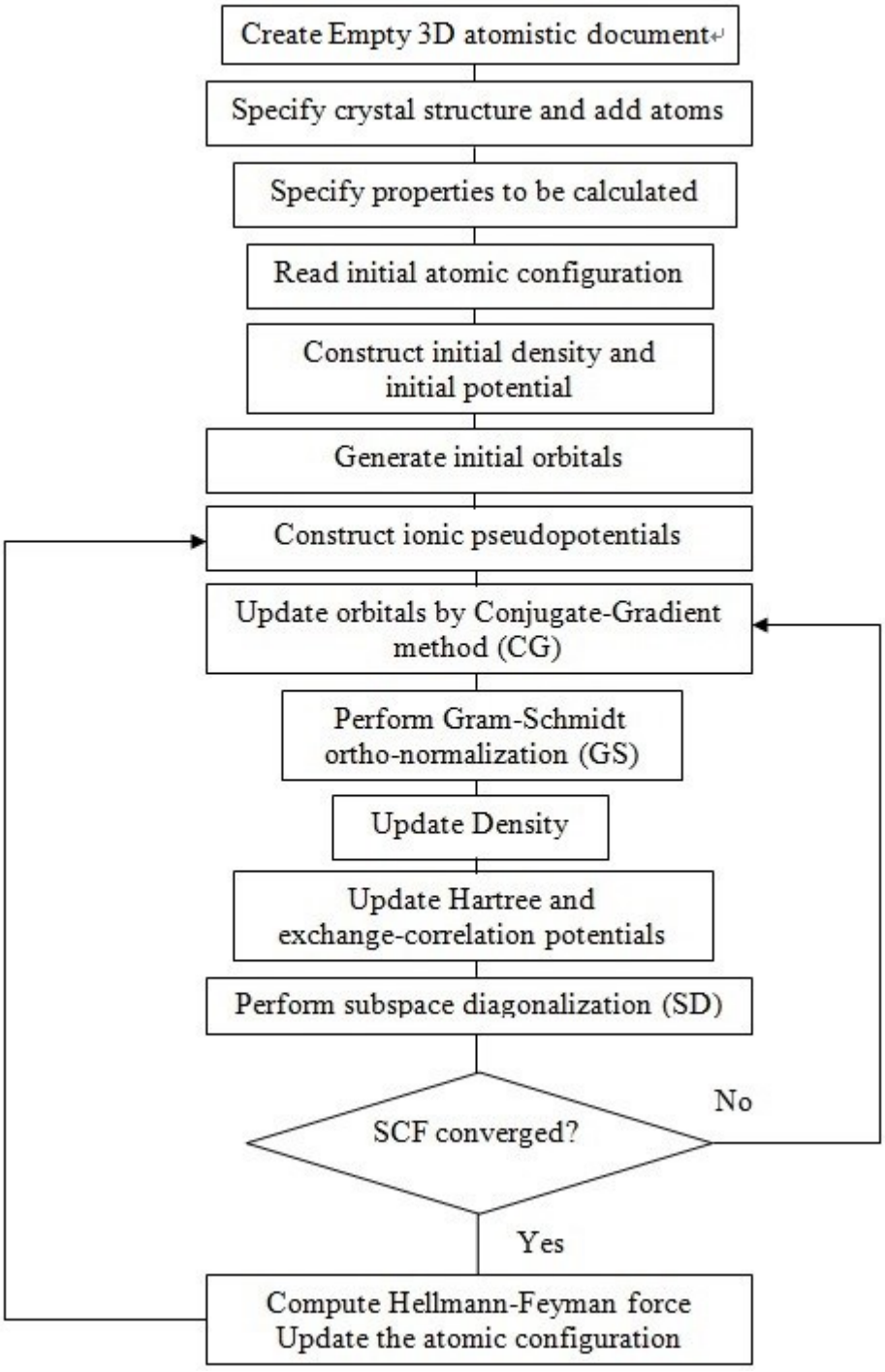

Figure 3.6 Flowchart of a CASTEP calculation [Adopted from 3.3]

3.2. Example of Yttrium Aluminum Garnet (YAG) Calculation

Create a new project in Material Studio. To generate a lattice create a new 3D atomistic document from the new shortcut menu then rename the .xsd document. From the build menu select the choose build crystal which opens up a Build crystal dialog shown below. In the case of YAG (Yttrium Aluminum Garnet), enter 230 for the space group. Then move to the lattice parameter tab to specify the initial lattice parameter of the crystal structure which is 12Å in this case. This creates an empty cube in the 3D atomistic document in which the atoms have to be added in. Selecting add atoms from the build menu will open up the add atom dialog. By opening up the periodic table any element can be added. In this case, Yttrium will be added with coordinates (0.125, 0, 0.25) which is dodecahedral (24c) site in Wyckoff position. Make sure that the coordinate system is in fractional from the options tab of the add atoms dialog. If an atom is added to a position Material Studio fills all the equivalent sites automatically. The figure shows all the Yttrium atoms filled in the lattice structure with the balls and stick display style. Add the rest of the atoms with octahedral (16a) site and tetrahedral (24d) site for Al atoms and (96h) site for O atoms. When all of the atoms are filled run a CASTEP calculation from the modules menu. First to optimize the structure change the task to the geometry optimization then click more to specify the optimization conditions. The electronic exchange-correlation functional energy was approximated with Generalized gradient approximation (GGA). Specify the calculation quality, in this case, ultra-fine quality was chosen then choose to optimize the cell with 100 maximum iterations. In the options tab the BFGS algorithm was chosen for this calculation.

Now move to the electronic part of the calculation. The energy cut-off and the k-point set were changed from default for this calculation by going in to the more… option in the electronics tab.The plane wave cutoff energy was chosen to be 450eV and from the k-point tab the 3x3x3 k-points mesh with Monkhorst-Pack method was chosen. From the properties tab, many kinds of properties can be selected to be included in the calculation. Band structure, Density of States and optical properties were included in this calculation. Options can also be changed for these calculations for properties by clicking more. Here the k-point set was again changed to 3x3x3 for the density of states calculation.

Finally the calculation can be started by stating computational options such as the number of cores to be used, optimization options, update intervals and etc. There are two options for runtime optimization, speed and memory. Memory optimization uses the full CPU power available whereas the speed optimization uses the full memory available. The job control option window will let more detailed adjustments to be made for the calculation. It is recommended to check the items in the live updates so that the user can see how the calculation is performing.

When the calculation starts several files will be created within the project containing the information about the properties that were asked to calculate along with the graphics that shows the progress of the geometry optimization iterations. The optimization convergence shows how each criterion which are energy change, maximum displacement, maximum force and maximum stress changed for each iteration step and how they converged to the targeted values.

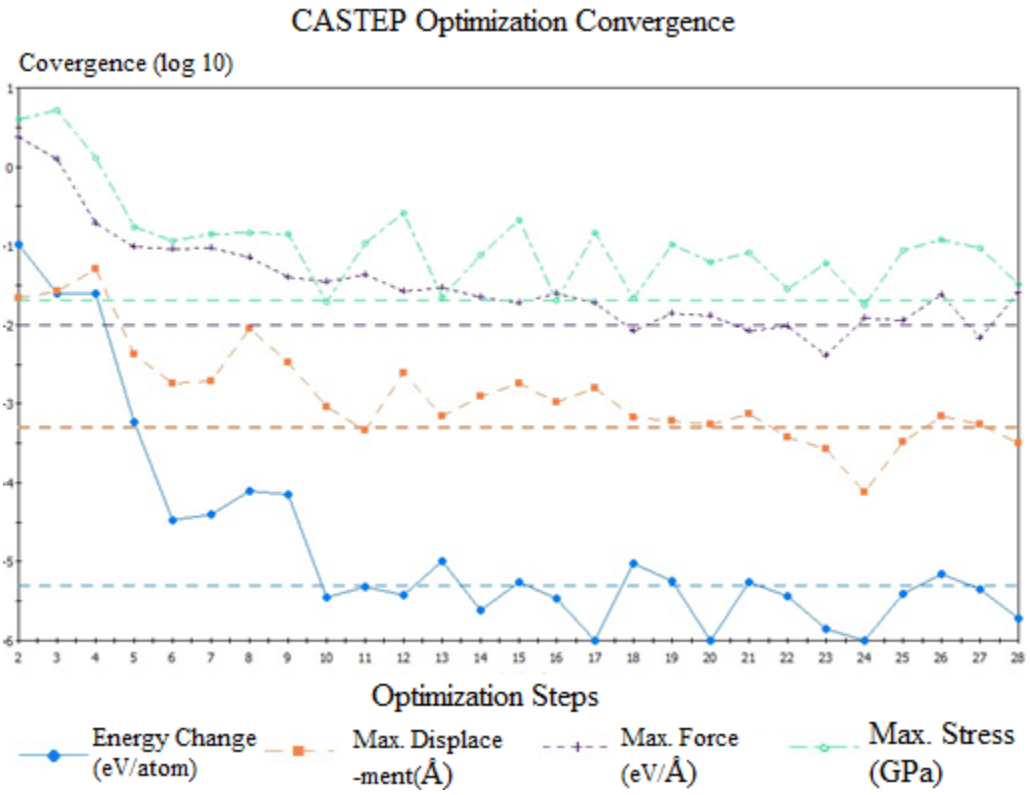

Figure 3.7. Optimization convergence graph of YAG

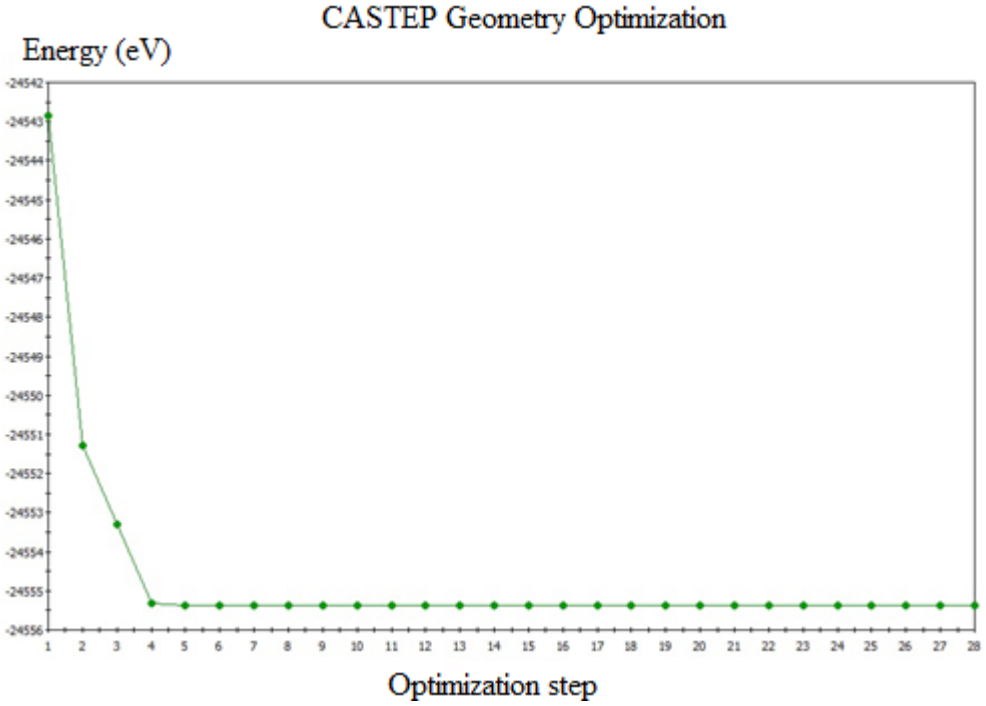

Figure 3.8. Energy of YAG system during geometry optimization iterations

References

[3.1] S. J. clark: *First principles methods using CASTEP*: Zeitschrift für Kristallographie. **220** 567-570 (2005)

[3.2] Material studio CASTEP online help (http://www.tcm.phy.cam.ac.uk/castep/documentation/WebHelp/CASTEP.html) (Updated: 2014) (Accessed: Apr 2015)

[3.3] T. Collis: *Porting the DFT code CASTEP to GPGPUs* (http://www.ccs.tsukuba.ac.jp/eng/wordpress/wp-content/uploads/2013/06/13-Toni-Collis.pdf) (Updated: 2013) (Accessed: Apr 2015)

CHAPTER 4

DFT CALCULATION RESULTS ON GARNET HOST LATTICES

4.1. Prior Informatics Screening on Garnets

For faster search of the optimum garnet host lattices that are improved self-activated scintillator materials, informatics analyses were performed on the two primary properties of interest: light yield and decay time. A database of descriptors associated with the constituent elements was used, with the descriptors capturing average pseudopotential radius, sum of atomic weights, average atomic density, Martynov-Batsanov electronegativity, average melting temperature, number of valence electrons per atom, first ionization potential and other similar descriptors known for all the elements. These descriptors were first screened to identify those most correlated with light yield and/or decay time.

A predictive informatics approach was then used to develop models for the two scintillator properties as a function of the descriptors, so that an equation of each property is developed such that the property equals a linear combination of the selected descriptors. After validating the model, the properties for the entire chemical search space can be calculated very rapidly. These two properties were calculated for 486 garnet host lattice chemistries. All of the combination of properties were looked at to identify the chemistries with improved combination. Through this approach, the 486 garnets were reduced to 12 garnets [4.1-4.3] with exceptional properties illustrated by Figure 4.1. The list of reduced 12 garnet host lattices are shown in table 4.1.

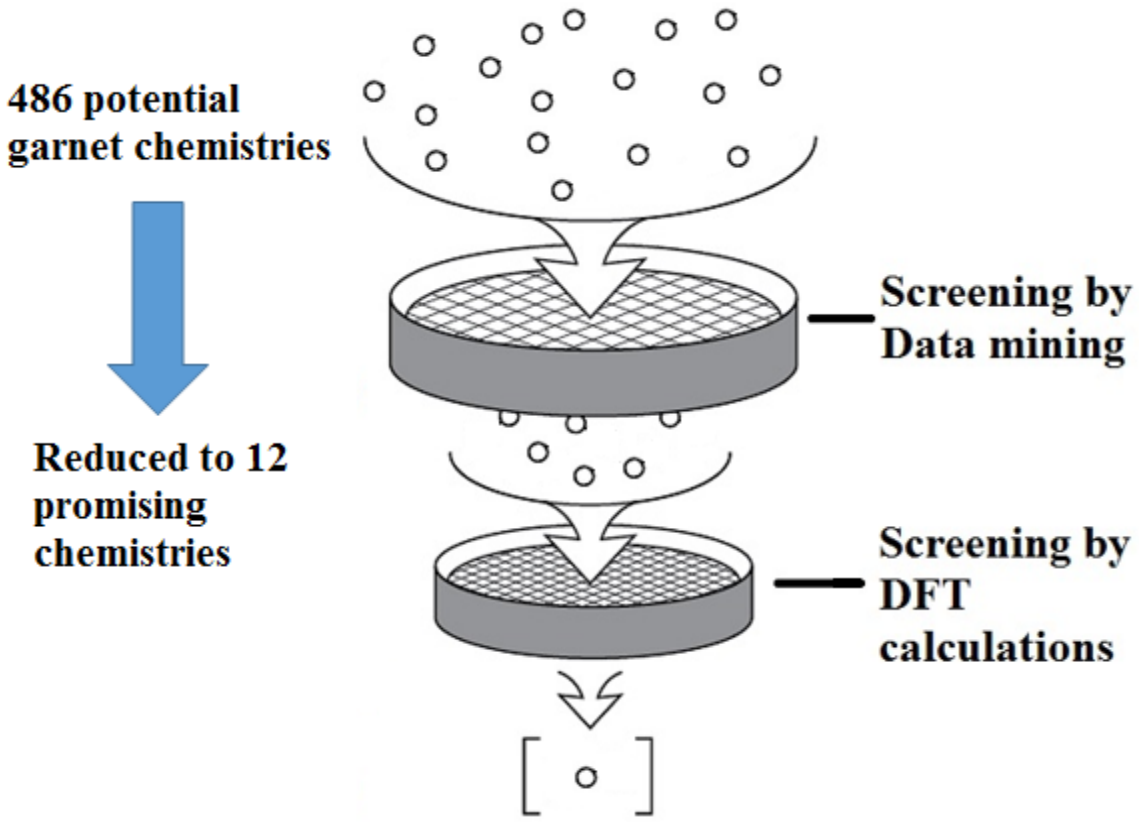

Figure 4.1. A schematic illustration of informatics screening step on garnet host lattices.

Table 4.1. List of 12 promising garnet host lattices after the informatics screening step.

$Y_2TbAl_2Ga_3O_{12}$	$Y_2DyAl_2Ga_3O_{12}$	$Y_2HoAl_2Ga_3O_{12}$	$Tb_3Al_2Ga_3O_{12}$
$Dy_3Al_2Ga_3O_{12}$	$Ho_3Al_2Ga_3O_{12}$	$Dy_2YAl_2Ga_3O_{12}$	$Y_2ErAl_2Ga_3O_{12}$
$Y_2TmAl_2Ga_3O_{12}$	$Y_2YbAl_2Ga_3O_{12}$	$Ho_2YAl_2Ga_3O_{12}$	$Er_2YAl_2Ga_3O_{12}$

While this approach identifies the chemistries with desired properties, it doesn't take the stability of the compounds into account. Therefore, the DFT calculations performed serve two functions: calculating the bandgap to see if it suggests exceptional light yield and identifying which of the compounds are stable.

4.2 Yttrium Aluminum Garnet (YAG)

DFT calculation was performed on $Y_3Al_5O_{12}$, which was previously identified as a garnet host lattice chemistry with the best combination for any garnet of high light yield and low decay time, in order to validate the informatics-aided prediction. Yttrium Aluminum Garnet crystallizes in a body-centered cubic structure with the formula $Y_3Al_5O_{12}$. Figure 4.2 shows the crystal structure of YAG. The unit cell belongs to the space group Ia3d (O_h^{10}) and contains 160 atoms.

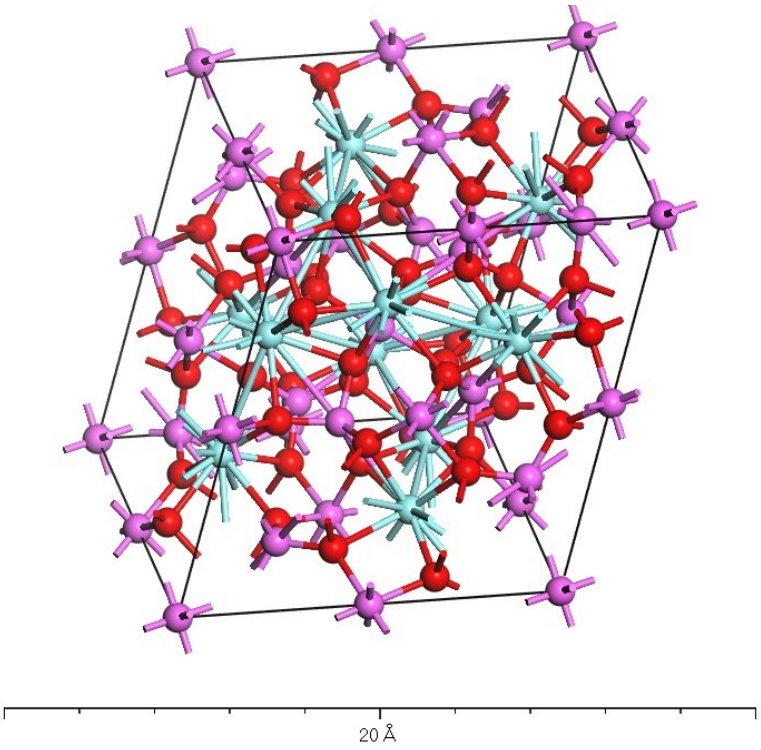

Figure 4.2. Unit cell structure of $Y_3Al_5O_{12}$ shown from CASTEP

The geometry optimization was initiated from the experimental crystal structure of YAG [4.4-4.5]. The unit cell structure built with the lattice constant of 12 Å followed the value reported by Geller [4.4]. The red atoms as oxygen atoms with coordinates (-0.0383, 0.0472,

0.1535) occupying (96h) were taken from the data reported by Prince [4.5]. Pink atoms as aluminum atoms taking (0, 0, 0) position with Wyckoff positions octahedral (16a) site. Aluminum atoms occupy tetrahedral (24d) site as well with coordinates of (0.375, 0, 0.25) position. The cyan colored atoms are the Yttrium atoms with input coordinates (0.125, 0, 0.25) in fractional coordinate system which is the dodecahedral (24c) site in Wyckoff notation with all the equivalent sites are automatically filled.

The cell was relaxed, and an energy cutoff of 450 eV was applied. The total energy code Cambridge sequential total energy package (CASTEP) was used for all the calculations. Geometrical optimization was performed to obtain the theoretical equilibrium crystal structure of $Y_3Al_5O_{12}$. The lattice constant and internal atomic coordinates were optimized independently to minimize the free enthalpy, inter-atomic forces and unit cell stresses. Within the first-principles calculations, the interaction between the ion cores and the electrons was represented by the Vanderbilt-type ultra-soft pseudopotential. The electronic exchange-correlation energy was treated under the generalized gradient approximation (GGA). The plane-wave basis set cutoff was set to 450 eV for all the calculations. Special points sampling integration over the Brillouin zone was employed by using the Monkhorst–Pack method with a 3x3x3 special k-points mesh. The Brodyden-Fletcher-Goldfarb-Shanno (BFGS) minimization scheme was used in geometrical optimization. The convergence criteria for the geometrical optimization are that the difference in total energy is within $5x10^6$ eV/atom, the maximum ionic Hellmann–Feynman force is within 0.01 eV/Å, the maximum ionic displacement is within $5x10^4$Å, and the maximum stress is within 0.02 GPa. These parameters lead to good convergence of the total energy and geometrical configuration. Using the converged unit cell structure, the band structure was calculated shown in figure 4.3.

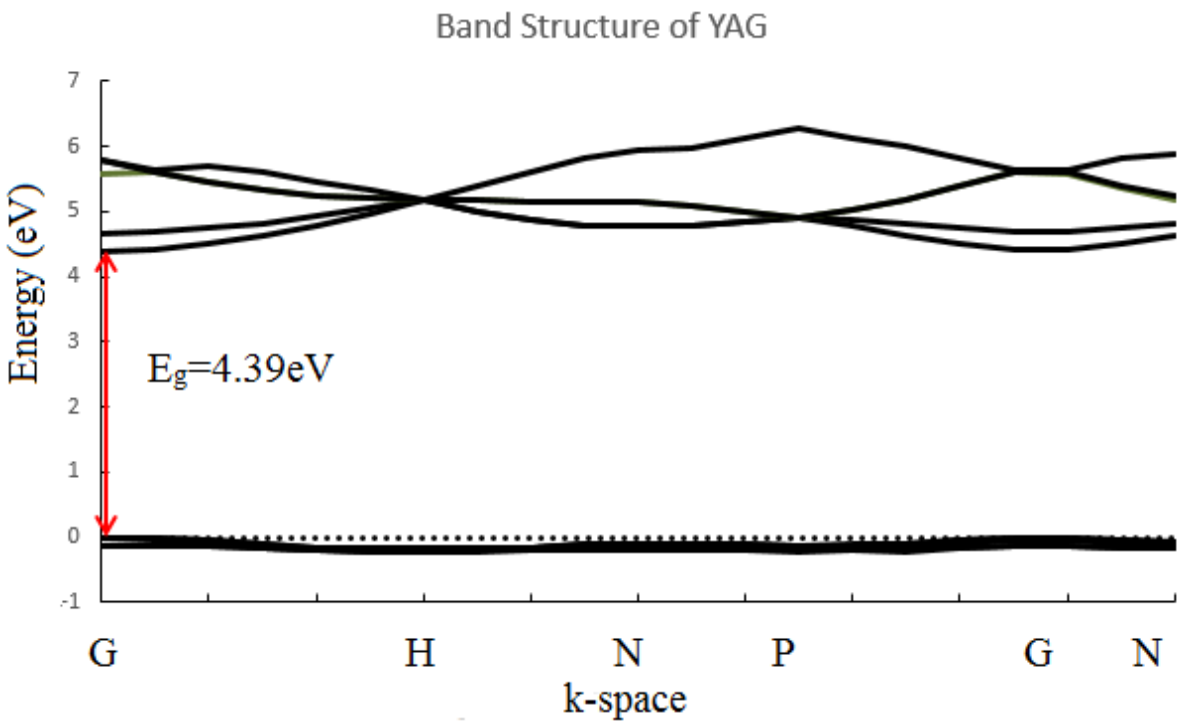

Figure 4.3. The band structure of Yttrium Aluminum Garnet.

The band gap from this band structure is calculated as 4.39 eV. Having developed the calculation approach, the band gap for the other exceptional garnet chemistries will be calculated. The output of the modeling can then be added to the informatics database in order to refine the modeling and identify additional scintillator host lattices.

The next figure, figure 4.4, shows the converged YAG cell after the calculation has been done. It shows the primitive cell with the stabilized lattice parameter of 10.39Å along with the Brillouin zone indicated with sky blue color outside of the cell. The red line shows the path that the band structure was calculated on including the high symmetry points. The g1, g2, g3 are axis for the reciprocal lattice.

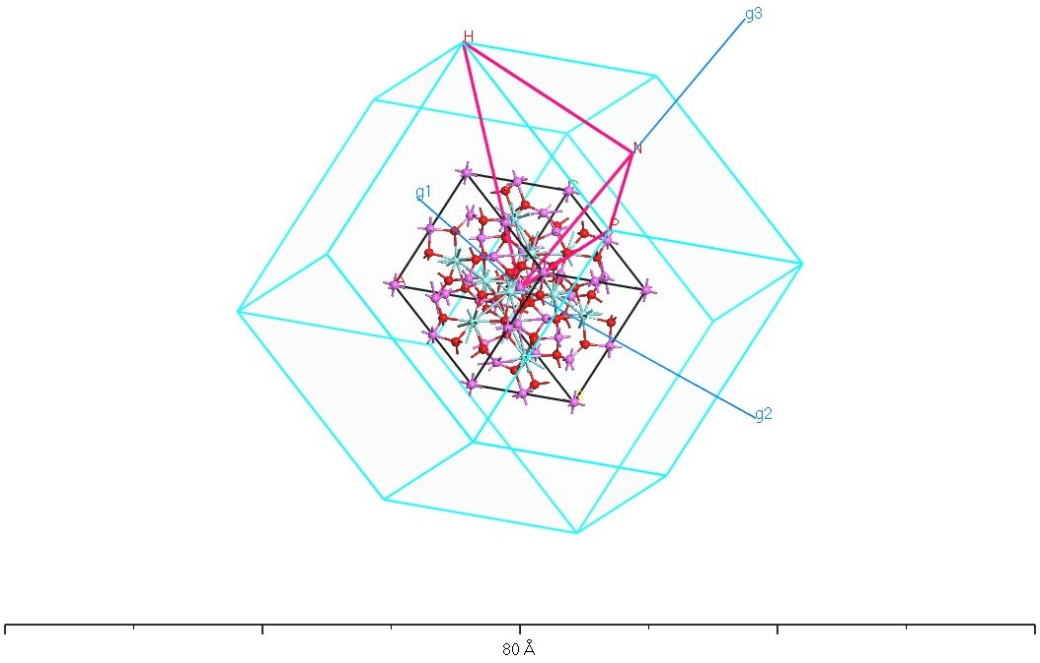

Figure 4.4 Converged YAG Structure

4.3. Terbium Aluminum Gallium Garnet

DFT calculation was performed on $Tb_3Al_2Ga_3O_{12}$, which was previously identified as a garnet host lattice chemistry with the best combination for any garnet of high light yield and low decay time, in order to validate the informatics-aided prediction. To achieve the light yield predicted for $Tb_3Al_2Ga_3O_{12}$, a band gap of ~ 3 eV is required. The unit cell was achieved through a close structure as shown in Figure 4.5.

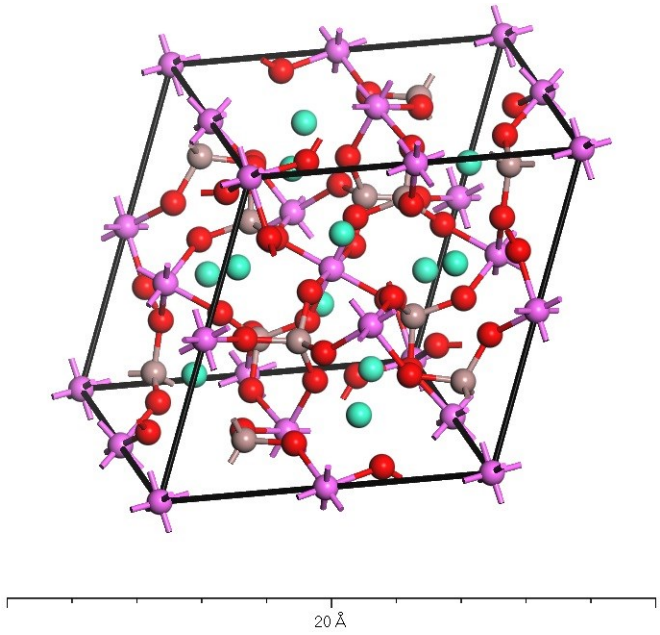

Figure 4.5 Unit cell structure of $Tb_3Al_2Ga_3O_{12}$, with Tb as green, Al as pink, Ga as brown, and O as red atoms.

The unit cell structure built with the red atoms as oxygen atoms with coordinates (-0.0383, 0.0472, 0.1535) occupying (96h), pink atoms as aluminum atoms taking (0, 0, 0) position with Wyckoff positions octahedral (16a) site. Gallium atoms (brown) occupy tetrahedral (24d) site with coordinates of (0.375, 0, 0.25) position instead of aluminum atoms in this structure site. The emerald green colored atoms are the Terbium atoms with input coordinates (0.125, 0, 0.25) in fractional coordinate system which is the dodecahedral (24c) site in Wyckoff notation with all the equivalent sites are automatically filled.

The cell was relaxed with identical calculation criteria with YAG. Geometrical optimization was performed to obtain the theoretical equilibrium crystal structure of $Tb_3Al_2Ga_3O_{12}$ with an energy cutoff of 450 eV. The lattice constant and internal atomic coordinates were optimized independently to minimize the free enthalpy, inter-atomic forces and unit cell stresses. Within the first-principles calculations, the interaction between the ion

cores and the electrons was represented by the Vanderbilt-type ultra-soft pseudopotential. The electronic exchange-correlation energy was treated under the generalized gradient approximation (GGA). The plane-wave basis set cutoff was set to 450 eV for all the calculations. Special points sampling integration over the Brillouin zone was employed by using the Monkhorst–Pack method with a 3x3x3 special k-points mesh. The Brodyden-Fletcher-Goldfarb-Shanno (BFGS) minimization scheme was used in geometrical optimization. The convergence criteria for the geometrical optimization are that the difference in total energy is within $5x10^6$ eV/atom, the maximum ionic Hellmann–Feynman force is within 0.01 eV/Å, the maximum ionic displacement is within $5x10^4$Å, and the maximum stress is within 0.02 GPa. These parameters lead to good convergence of the total energy and geometrical configuration. Using the converged unit cell structure, the band structure was calculated shown in figure 4.6 and the band gap is calculated as ~0.742 eV.

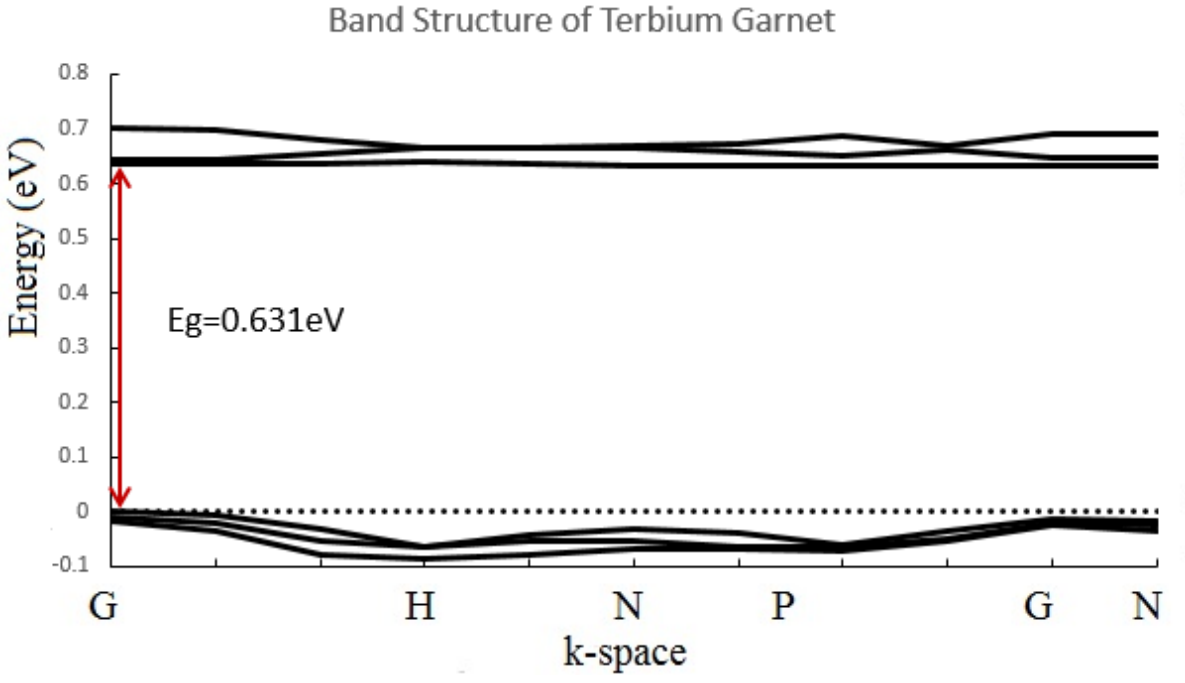

Figure 4.6. Band Structure of $Tb_3Al_2Ga_3O_{12}$.

4.4. Summary of Garnet Host Lattice Design

As a result of the DFT calculations on garnets, out of 12 informatics predicted promising garnet class scintillator materials, only Terbium Aluminum Gallium Garnet ($Tb_3Al_2Ga_3O_{12}$) is identified as a promising garnet host lattice. Figure 4.7 shows where $Tb_3Al_2Ga_3O_{12}$ sits in the plot of previously known garnet structures.

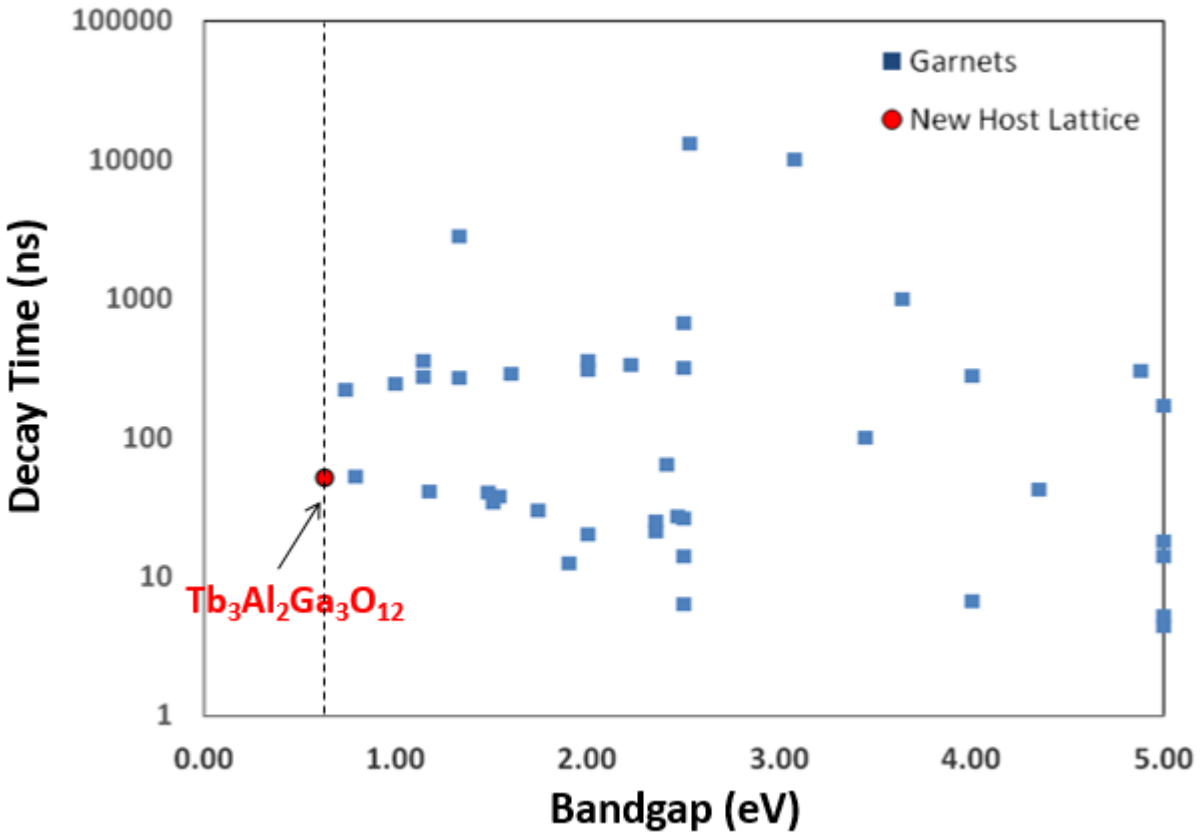

Figure 4.7. Decay time and light yield of new $Tb_3Al_2Ga_3O_{12}$ garnet plotted to be compared with previously known garnet structures.

The calculated band gap of $Tb_3Al_2Ga_3O_{12}$ garnet is smaller than other garnet host lattices which meets the design requirement of pushing boundary for bandgap and light yield. The fact that it has a direct bandgap also contributes to improving the efficiency of the scintillator.

References

[4.1] S. Broderick and K. Rajan: *Informatics derived materials databases for multifunctional properties*: Science and Technology of Advanced Materials **16** 013501 (2015)

[4.2] S. Ganguly, C.S. Kong, S. Broderick, K. Rajan: *Informatics-Based Uncertainty Quantification in the Design of Inorganic Scintillators*: Materials and Manufacturing Processes **28** 726-732 (2013)

[4.3] C.S. Kong, K. Rajan: *Rational Design of Binary Halide Scintillators via Data Mining*: Nuclear Instruments and Methods in Physics Research **680** 145-154 (2012)

[4.4] S. Geller et al.: *Thermal expansion of yttrium and gadolinium iron, gallium and aluminum garnets*: Journal of Applied Cystallography **2** 86-88 (2013)

[4.5] E. Prince: *Neutron Diffraction Measurements on Yttrium-Iron and Yttrium-Aluminum Garnets*: Acta Crystallographica **10** 35 (1957)

CHAPTER 5

DFT CALCULATION RESULTS ON CO-DOPED PEROVSKITES

5.1. Advantage of Doping

In addition to trying new materials, doping a known material can be an excellent way to design a scintillator. Doped element changes the electronic configuration of the materials which affects the light yield. When dopants are added they generate oxygen interstitials that reduce the oxygen vacancy concentration through a Frenkel-pair recombination. It is good to reduce the oxygen vacancy concentration because these oxygen vacancies limit the scintillation properties by trapping electrons in the system, in other words limiting the energy transport efficiency S. Doping the scintillation material also increases the density of the material which also enhances the scintillation properties.

5.2. Prior Informatics Screening on Perovskites

For perovskites, informatics designing step is again applied to quickly reduce down to the optimum perovskite co-dopants. Since we are using dopants, unlike garnets, informatics analyses were performed on the five lowest energy mechanisms describing defects in perovskites when they are co-doped with tetravalent cations. The five lowest energy mechanisms are shown in Equation 5.1 to 5.5 [5.1]

$$2MO_2 + 2RE_{RE}^{X} + Al_{Al}^{X} \Leftrightarrow 2M_{RE}^{\bullet} + O_i^{''} + RE_{Al}^{X} + REAlO_3 \quad (5.1)$$

$$2MO_2 + RE_{RE}^{X} + 2Al_{Al}^{X} \Leftrightarrow 2M_{Al}^{\bullet} + O_i^{''} + Al_{RE}^{X} + REAlO_3 \quad (5.2)$$

$$2MO_2 + RE_{RE}^{X} + Al_{Al}^{X} \Leftrightarrow M_{RE}^{\bullet} + M_{Al}^{\bullet} + O_i^{''} + REAlO_3 \quad (5.3)$$

$$3MO_2 + 2RE_{RE}^{X} + 2Al_{Al}^{X} \Leftrightarrow 2M_{Al}^{\bullet} + M_{RE}^{\bullet} + V_{RE}^{''} + 2REAlO_3 \quad (5.4)$$

$$3MO_2 + 2RE_{RE}^{X} + 2Al_{Al}^{X} \Leftrightarrow 2M_{RE}^{\bullet} + M_{Al}^{\bullet} + V_{Al}^{''} + 2REAlO_3 \quad (5.5)$$

The correlation between defect reaction energies and the descriptors of co-dopant elements (i.e. electronegativities, ionization potentials and radii) were identified and validated so that an equation of each defect reaction energy is a linear combination of the selected descriptors. With these equations we find co-dopant schemes that favor the reaction equations (5.1), (5.2) and (5.3) because those defect reactions creates oxygen interstitials which reduces the oxygen vacancy concentration which in turn improves scintillation performance. Through this approach, about 700 potential co-dopant chemistries garnets were reduced to 26 with exceptional properties illustrated by Figure 5.1. Each pair of spheres represents a possible co-dopant combination pair that can be doped into $YAlO_3$ perovskite structure. The list of reduced 26 promising co-dopant combinations are shown in table 5.2[5.1].

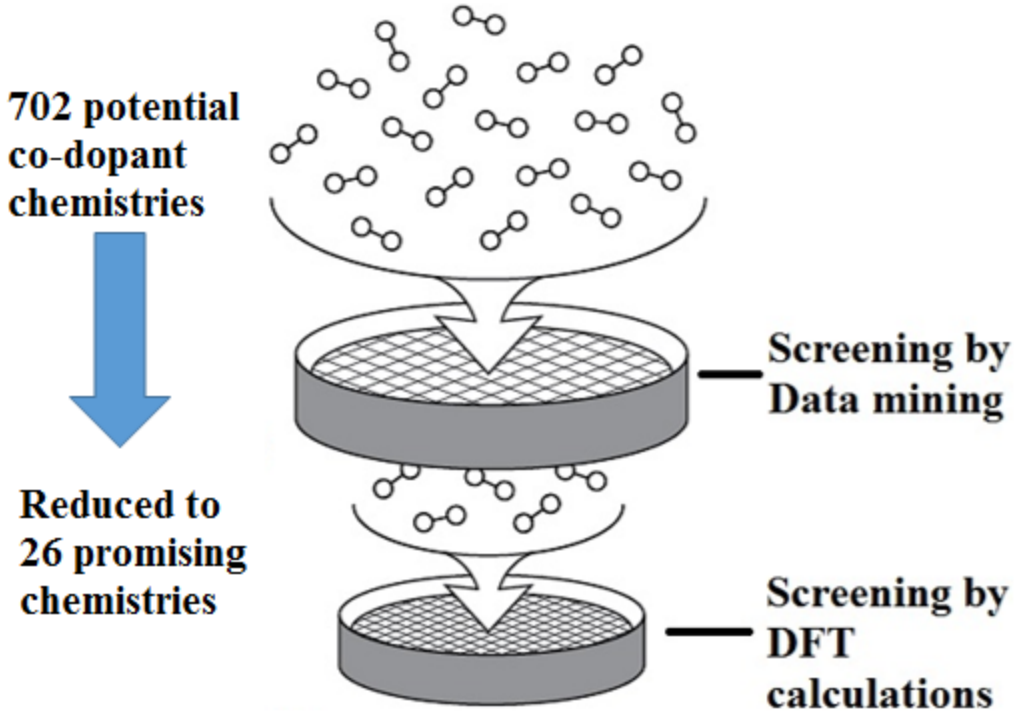

Figure 5.1. A schematic illustration of informatics screening step on perovskite co-dopant chemistries.

Table 5.2. List of 26 promising perovskite co-dopant chemistries after the informatics screening step.

YAP: Ce, Ge	YAP: Pr, Ge	YAP: Ce, W	YAP: Pr, W
YAP: Ce, V	YAP: Pr, V	YAP: Ce, Mo	YAP: Pr, Mo
YAP: Ce, Fe	YAP: Pr, Fe	YAP: Ce, Ta	YAP: Pr, Ta
YAP: Ce, Ti	YAP: Pr, Ti	YAP: Ce, Nb	YAP: Pr, Nb
YAP: Ce, Mn	YAP: Pr, Mn	YAP: Ce, Zr	YAP: Pr, Zr
YAP: Ce, Cr	YAP: Pr, Cr	YAP: Ce, Hf	YAP: Pr, Hf
YAP: Ce, Co	YAP: Pr, Co		

While this approach identifies the chemistries with desired properties, it doesn't take the stability of the compounds into account. Therefore, the DFT calculations performed serve two functions: calculating the bandgap to see if it suggests exceptional light yield and identifying which of the compounds are stable.

5.3. Yttrium Aluminum Perovskite (YAP)

Before performing DFT calculations doped Yttrium Aluminum Perovskites (YAP), DFT calculation was performed for an undoped YAP. $YAlO_3$ crystal crystallizes in the orthorhombically distorted perovskite structure. Figure 5.2 shows the crystal structure of YAP. With the unit cell belonging to the space group Pbnm (D_{2h}^{16}). Lattice parameters are as follows: a_1: 5.180 Å, a_2: 5.330 Å, a_3: 7.375 Å, whereas their atomic coordinates are Y with coordinates (-0.0104, 0.0526, 0.25) (occupying 4c), Al with coordinates (0.5, 0, 0) (occupying 4b), O atoms with coordinates (0.086, 0.475, 0.25) (4c) and (-0.297, 0.293, 0.044) (8d) [5.2].

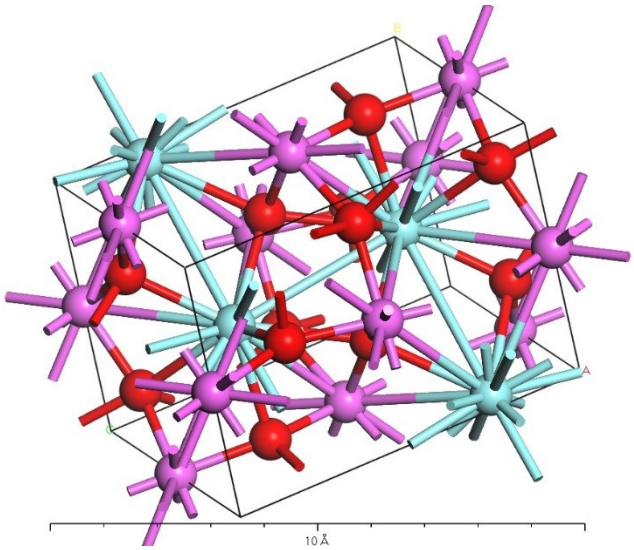

Figure 5.2. Unit cell Structure of YAP with Y as cyan, Al as pink, and O as red atoms.

The cell was relaxed, and an energy cutoff of 450 eV was applied. Geometrical optimization was performed to obtain the theoretical equilibrium crystal structure of $YAlO_3$. The lattice constant and internal atomic coordinates were optimized independently to minimize the free enthalpy, inter-atomic forces and unit cell stresses. Within the first-principles calculations, the interaction between the ion cores and the electrons was represented by the Vanderbilt-type ultra-soft pseudopotential. The electronic exchange-correlation energy was treated under the generalized gradient approximation (GGA). The plane-wave basis set cutoff was set to 450 eV for all the calculations. Special points sampling integration over the Brillouin zone was employed by using the Monkhorst–Pack method with a 3x3x3 special k-points mesh. The Brodyden-Fletcher-Goldfarb-Shanno (BFGS) minimization scheme was used in geometrical optimization. The convergence criteria for the geometrical optimization are that the difference in total energy is within $5x10^6$ eV/atom, the maximum ionic Hellmann–Feynman force is within 0.01 eV/Å, the maximum ionic displacement is within $5x10^4$Å, and the maximum stress is within 0.02 GPa. These parameters lead to good convergence of the total energy and geometrical configuration. Using the converged unit cell structure, the band structure was calculated shown in figure 5.3.

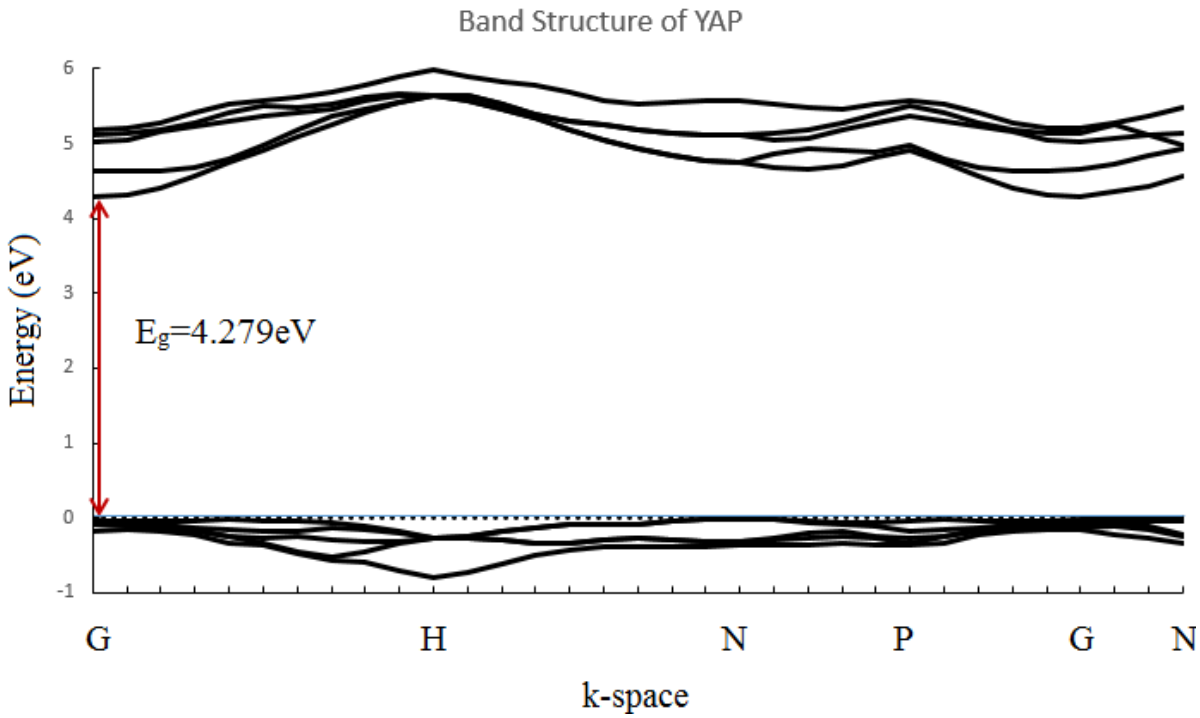

Figure 5.3. Band Structure of YAP

The band gap from this band structure of YAP, figure 5.3, is calculated to be 4.28 eV. Having developed the calculation approach, the band gap for the other co-doped perovskite chemistries will be calculated. The output of the modeling can then be added to the informatics database in order to refine the modeling and identify additional scintillator host lattices.

5.4. Co-doped Yttrium Aluminum Perovskites

DFT calculations were performed on multiple co-doped Yttrium Aluminum Perovskites with identical calculation parameters as undoped YAP except that two of Yttrium atoms were substituted with the dopants.

Crystal structure of YAP was created with unit cell belonging to the space group Pbnm (D_{2h}^{16}) and with lattice parameters (5.180 Å, 5.330 Å, 7.375 Å). The atomic coordinates are Y with coordinates (-0.0104, 0.0526, 0.25) (occupying 4c), Al with coordinates (0.5, 0, 0) (occupying 4b), O atoms with coordinates (0.086, 0.475, 0.25) (4c) and (-0.297, 0.293, 0.044) (8d) with two of the Y atoms substituted with co-dopants [5.2].

The cell was relaxed, and an energy cutoff of 450 eV was applied. Geometrical optimization was performed to obtain the theoretical equilibrium crystal structure of co-doped $YAlO_3$. The lattice constant and internal atomic coordinates were optimized independently to minimize the free enthalpy, inter-atomic forces and unit cell stresses. Within the first-principles calculations, the interaction between the ion cores and the electrons was represented by the Vanderbilt-type ultra-soft pseudopotential. The electronic exchange-correlation energy was treated under the generalized gradient approximation (GGA). The plane-wave basis set cutoff was set to 450 eV for all the calculations. Special points sampling integration over the Brillouin zone was employed by using the Monkhorst–Pack method with a 3x3x3 special k-points mesh. The Brodyden-Fletcher-Goldfarb-Shanno (BFGS) minimization scheme was used in geometrical optimization. The convergence criteria for the geometrical optimization are that the difference in total energy is within $5x10^6$ eV/atom, the maximum ionic Hellmann–Feynman force is within 0.01 eV/Å, the maximum ionic displacement is within $5x10^4$Å, and the maximum stress is within 0.02 GPa. These parameters lead to good convergence of the total energy and geometrical configuration.

After a series of calculations four systems were found to be stable. Using the final converged structures, calculated band gaps of YAP:Ce,Ta; YAP: Ce,Co ; YAP:Pr,Ti and YAP:Pr,W are shown in figures 5.4-5.7.

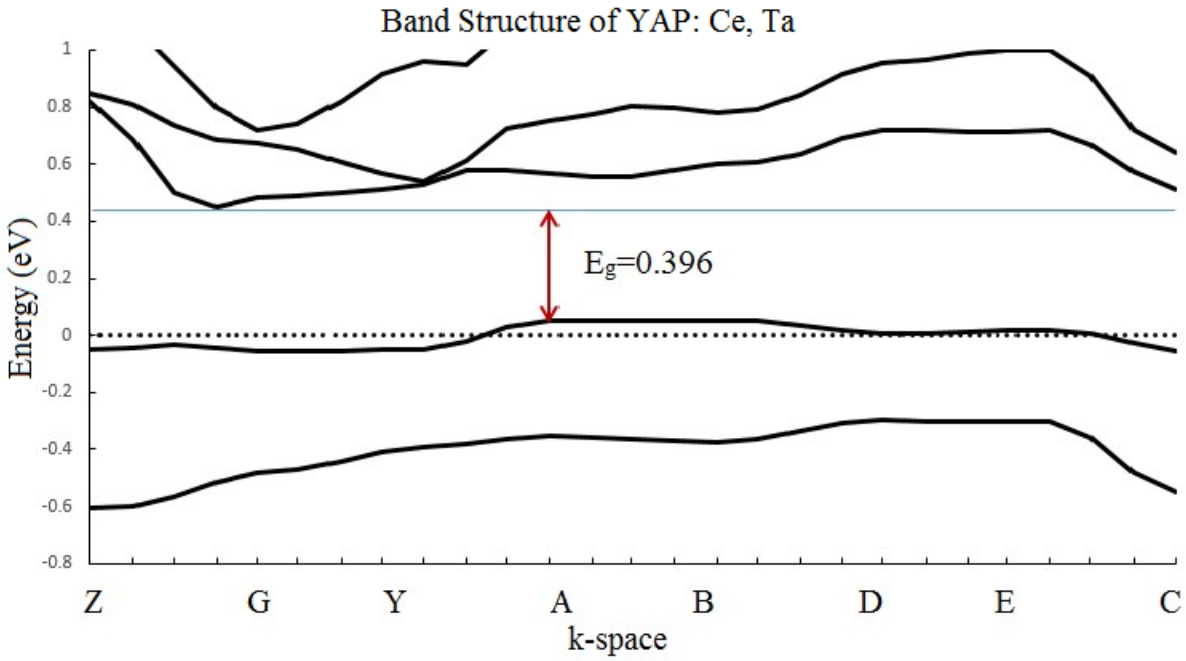

Figure 5.4. Band Structure of YAP:Ce,Ta.

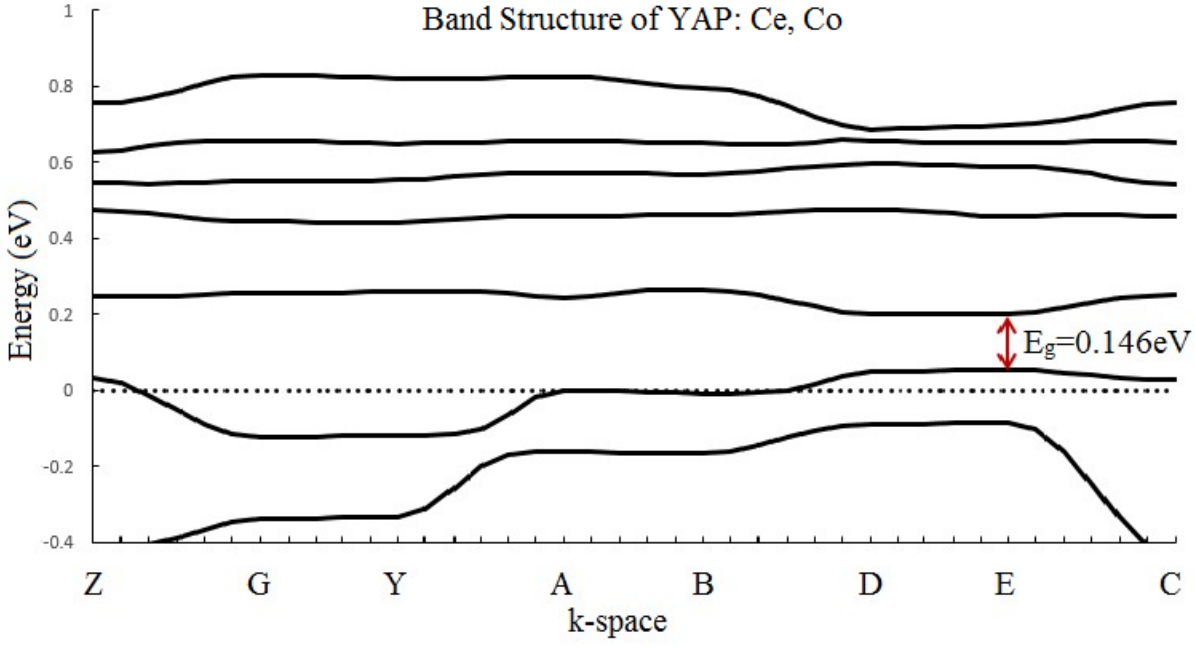

Figure 5.5. Band Structure of YAP:Ce,Co

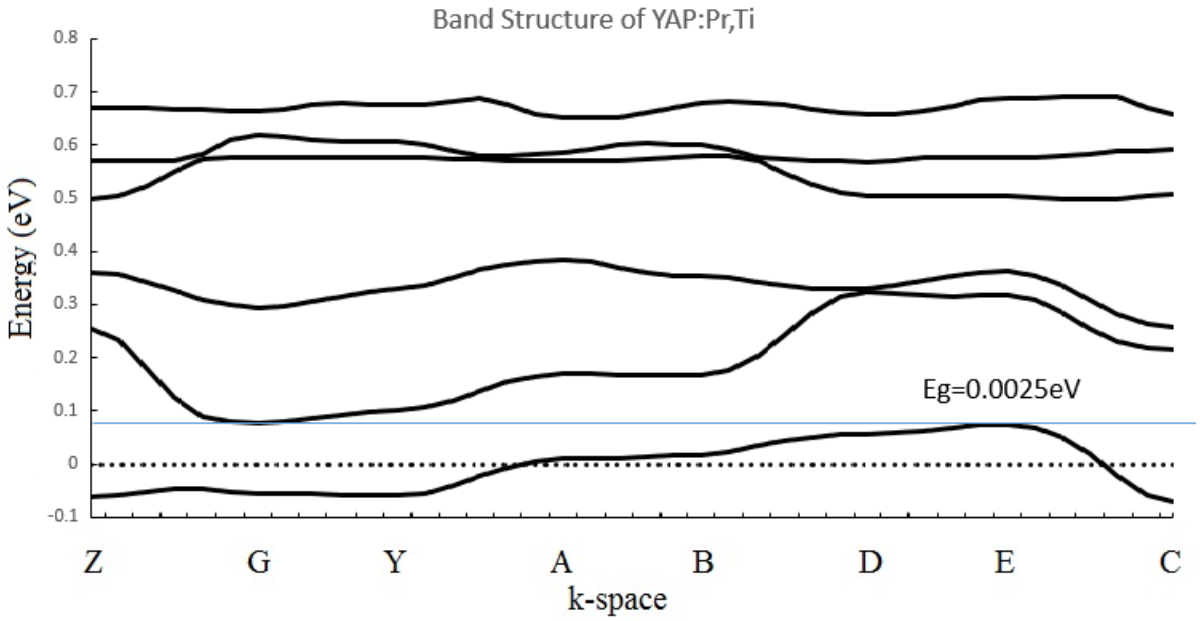

Figure 5.6. Band Structure of YAP:Pr,Ti

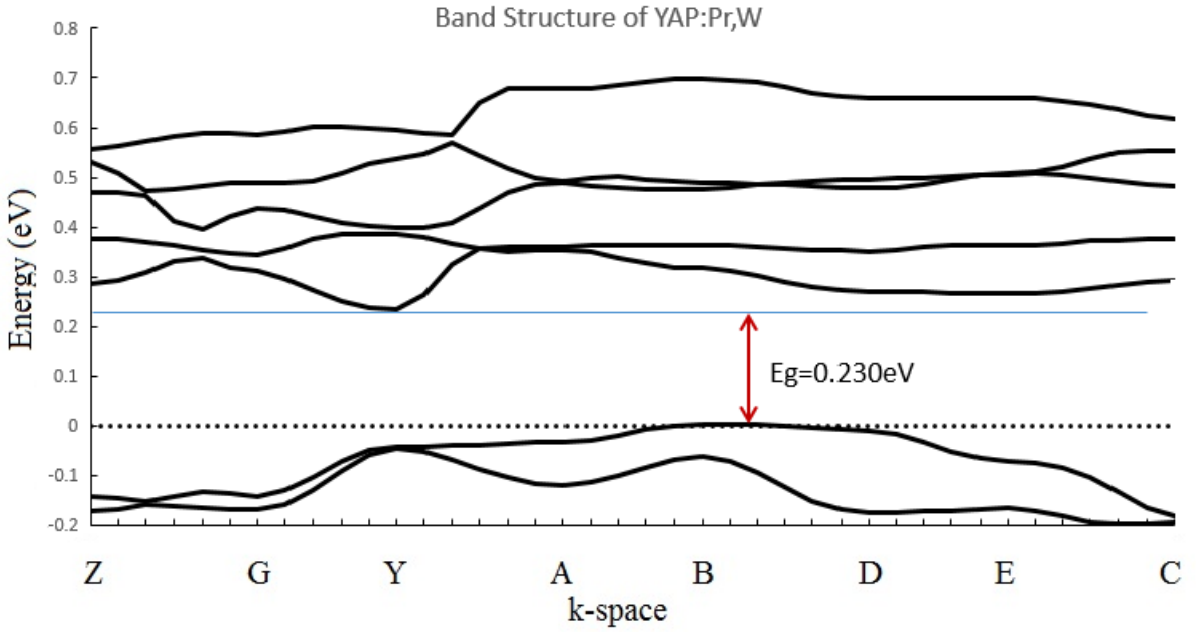

Figure 5.7. Band Structure of YAP:Pr,W

As a result of the DFT calculations on perovskite structures, YAP: Ce,Co, YAP: Pr, Ti, YAP: Pr,W and YAP: Ce,Ta made significant improvements over single doped pervoskites and stayed stable at the same time. Although YAP: Pr,Ti has smaller bandgap than YAP: Ce,Co, YAP: Ce,Co has a direct bandgap and therefore it has higher scintillator efficiency. The direct band gap is shown in the band structure Figure 5.5. Although DFT calculations approximate the band gaps to be lower than the experimental values, all of calculated codopant combination of YAP systems had very low band gaps suggesting a possibility of discovery of high light yield materials. Figure 5.10 shows the newly identified co-doped YAP systems plotted with other perovskite structures. They show much smaller bandgaps than other perovskite systems landing well inside the design target region. The decay time values used are the measured values of singly doped YAP:Ce and YAP:Pr.

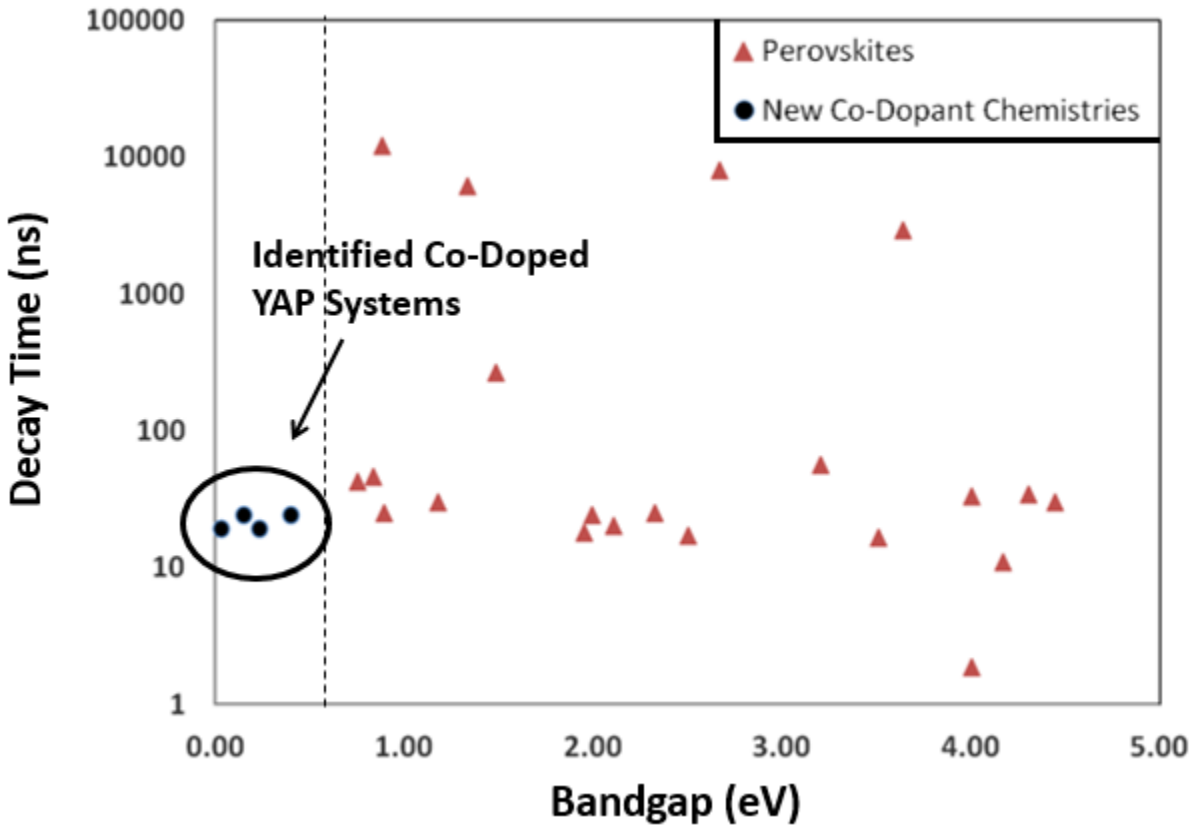

Figure 5.8. Newly identified co-dopant chemistries of YAP systems are plotted to be compared with previously known perovskite structures.

References

[5.1] P. Balachandran, C.S. Kong, S. Broderick, K. Rajan: *Informatics Based Modeling of Defect Reactions in Perovskite Scintillators*: (2015)

[5.2] D. M. Bercha et al.: *Elementary energy bands in ab intitio calculations of the $YAlO_3$ and SbSI crystal band structure*: Physical review B **66**, 195203 (2002)

CHAPTER 6

SUMMNARY AND CONCLUSIONS

The results of density functional calculation of band gaps of stable systems are summarized in the table 6.1 below.

Table 6.1. Summary of band gaps of calculated stable garnet and perovskite systems.

System	Band Gap (eV)
Yttrium Aluminum Garnet ($Y_3Al_5O_{12}$)	4.38
Terbium Aluminum Gallium Garnet (Tb3Al2Ga3O12)	0.631
Yttrium Aluminum Perovskite ($YAlO_3$)	4.32
Cerium doped YAP ($YAlO_3$:Ce)	0.734
Cerium, Tatalum codoped YAP ($YAlO_3$:Ce,Ta)	0.396
Cerium, Cobalt codoped YAP ($YAlO_3$:Ce,Co)	0.146
Praseodymium, Titanium codoped YAP ($YAlO_3$:Pr,Ti)	0.0025
Praseodymium, Tungsten codoped YAP ($YAlO_3$:Pr,W)	0.230

As a conclusion, previously unexplored garnet host lattices and co-dopant chemistries of perovskites were computationally explored. The major contribution of my research was that Terbium garnet host lattice was identified as improved garnet host lattice. Moreover, for perovskite co-dopant chemistries, 4 were identified as improved co-dopant schemes. They all fall into the target area and the scintillator materials with less than 1eV regime have been discovered for the first time, shown in Figure 6.1.

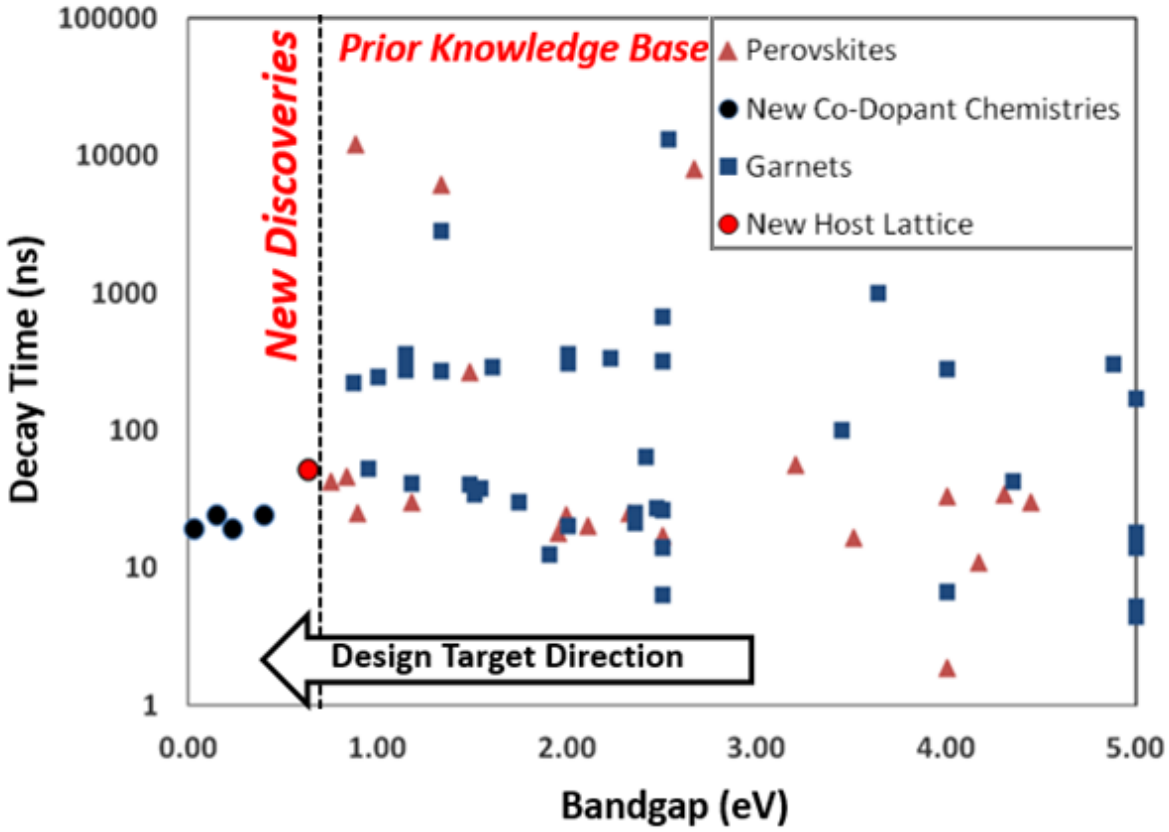

Figure 6.1. Decay time and light yield of newly identified garnet and co-doped YAP systems plotted with other garnets and perovskites.

Finally, more calculations can always be run for other possible compounds with more accurate settings to contribute for creating and improving a data set for informatics predicted inorganic scintillators. Furthermore, the methodology that combines the informatics predictions and DFT calculations can be extended beyond inorganic scintillator materials to materials including semiconductors and organic materials.